Provided for non-commercial research and educational use only.
Not for reproduction or distribution or commercial use.

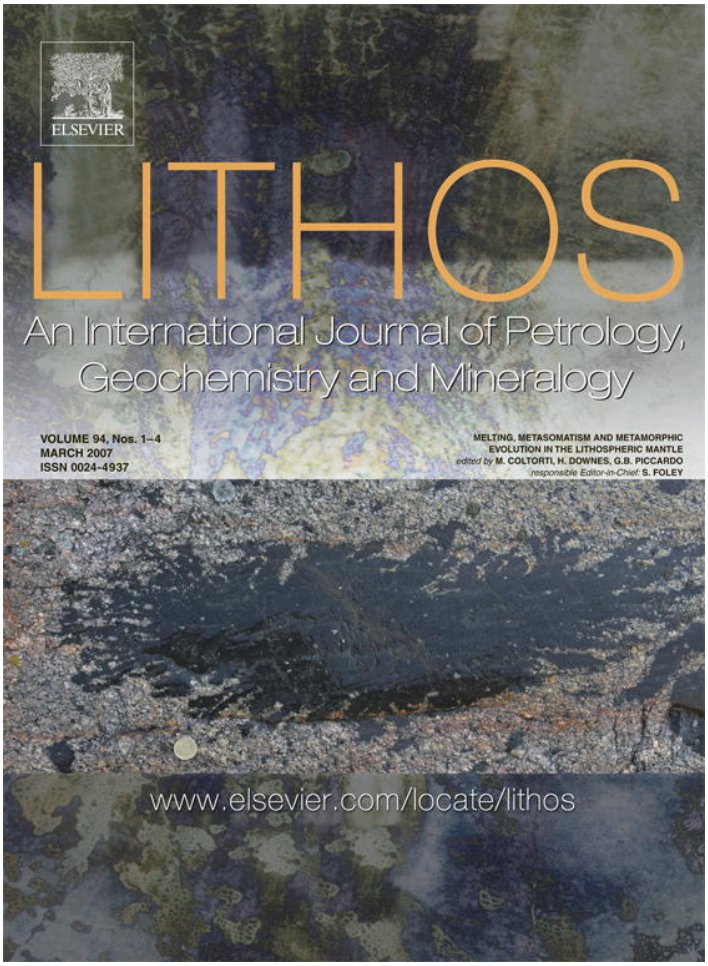

This article was originally published in a journal published by Elsevier, and the attached copy is provided by Elsevier for the author's benefit and for the benefit of the author's institution, for non-commercial research and educational use including without limitation use in instruction at your institution, sending it to specific colleagues that you know, and providing a copy to your institution's administrator.

All other uses, reproduction and distribution, including without limitation commercial reprints, selling or licensing copies or access, or posting on open internet sites, your personal or institution's website or repository, are prohibited. For exceptions, permission may be sought for such use through Elsevier's permissions site at:

http://www.elsevier.com/locate/permissionusematerial

Available online at www.sciencedirect.com
ScienceDirect
Lithos 94 (2007) 111–131
LITHOS
www.elsevier.com/locate/lithos

The effect of the Fernando de Noronha plume on the mantle lithosphere in north-eastern Brazil

Giorgio Rivalenti [a,*], Alberto Zanetti [c], Vicente A.V. Girardi [b], Maurizio Mazzucchelli [a], Colombo C.G. Tassinari [b], Gustavo W. Bertotto [d]

[a] *Dipartimento di Scienze della Terra, Università di Modena e Reggio Emilia, P.le S. Eufemia 19, 41100 Modena, Italy*
[b] *Instituto de Geociências, Universidade de São Paulo, Rua do Lago 563, Cidade Universitaria 05508-900, São Paulo, Brazil*
[c] *Dipartimento di Scienze della Terra, Università di Pavia and CNR, Istituto di Geoscienze e Georisorse, sezione di Pavia, Via Ferrata 1, 27100 Pavia, Italy*
[d] *CONICET and Facultad de Ciencias Exactas y Naturales, Universidad Nacional de La Pampa, Uruguay 151, 6300 Santa Rosa, La Pampa, Argentina*

Received 4 May 2005; accepted 2 June 2006
Available online 8 September 2006

Abstract

New xenolith occurrences in the Cenozoic alkali basalts of north-eastern Brazil have been studied in order to constrain the possible imprint on the continental mantle lithosphere of its passage over the Fernando de Noronha plume and the regional mantle processes. Texturally, the lherzolite and harzburgite xenoliths define three groups: *group 1*, porphyroclastic; *group 2*, protogranular; *group 3*, transitional between *groups 1* and *2*. Equilibrium temperatures are highest for *group 1* and lowest for *group 2*. Clinopyroxenes from *group 1* peridotites have Primitive Mantle (PM)-normalised REE patterns varying from L-MREE-enriched convex-upward, typical of phases in equilibrium with alkaline melts, to LREE-enriched, spoon-shaped, to LREE-enriched, steadily fractionated in a wehrlite. *Group 2* clinopyroxenes show patterns slightly depleted in LREE to nearly flat. The M-HREE are at 3–5 ×PM concentration level, as typical in fertile lithospheric lherzolites. Most of *group 3* clinopyroxenes show LREE-depleted patterns similar to the *group 2* ones, but in two samples the clinopyroxenes are characterised by LREE-enriched, spoon-shaped profiles. Sr and Nd isotopes of the *group 1* clinopyroxenes form an array between DM and EMI-like components, both of them are also present in the host basalts. Melts estimated to be in equilibrium with the *group 1* clinopyroxenes having L-MREE-enriched, convex-upward patterns are similar to the Cenozoic alkaline magmas. The *groups 2* and *3* clinopyroxenes define two distinct compositional fields at higher $^{143}Nd/^{144}Nd$ values, correlated with their LREE composition. The isotopes of the *groups 2* and *3* LREE-depleted clinopyroxenes form an array from DM towards the isotopic composition of Mesozoic tholeiitic basalts from north-eastern Brazil. Melts in equilibrium with these clinopyroxenes are similar to these basalts, thus suggesting that such xenoliths record geochemical imprint from older melt-related processes.

The LREE-enriched spoon-shaped *group 3* clinopyroxenes are characterised by the highest $^{143}Nd/^{144}Nd$ values at any given $^{87}Sr/^{86}Sr$ composition. These results are interpreted in terms of a lithospheric mantle section which underwent thermo-chemical and mechanical erosion by infiltration of asthenospheric alkali basalts having EMI-like isotope characteristics during Cenozoic time. At that time, the lithospheric mantle consisted of fertile lherzolites and harzburgites recording the geochemical imprint of Mesozoic mantle processes. The onset of the interaction between lithospheric peridotites and alkaline melts was characterised by the porous

* Corresponding author. Tel.: +39 59 2055813; fax: +39 59 2055898.
E-mail address: riva@unimore.it (G. Rivalenti).

0024-4937/$ - see front matter © 2006 Elsevier B.V. All rights reserved.
doi:10.1016/j.lithos.2006.06.012

Author's personal copy

flow percolation of small melt volumes that induced chromatographic enrichments in highly incompatible elements and the isotope signature of the spoon-shaped, *group 3* clinopyroxenes. *Group 1* peridotites represent the base of the lithospheric column eroded by the ascending alkaline melts, whereas the *group 2* documents the shallower lithospheric section, with *group 3* being the transition. The similarity of processes and isotope components in the protogranular xenoliths from Fernando de Noronha area and north-eastern Brazil supports the hypothesis that the lithosphere beneath Fernando de Noronha is a detached portion of the continental one. Furthermore, the similarity in terms of textural and geochemical features documented by the mantle samples coming from the two different regions seems to confirm the interference of the two regions with the same plume.
© 2006 Elsevier B.V. All rights reserved.

1. Introduction

Cenozoic alkali basalt centres in north-eastern Brazil are believed to represent the surface track of the passage of the craton over the Fernando de Noronha plume (O'Connor and Duncan, 1990). Gerlach et al. (1987) and Fodor et al. (1998) recognised in the Fernando de Noronha lavas three isotopic components: DM, EMII and HIMU (mantle end-members from Zindler and Hart, 1986). Fodor et al. (1998) emphasised that the Rio Grande do Norte alkali basalts derived from mixing of asthenospheric melts, largely of HIMU and DM characteristics, and EMI lithospheric components. At present, isotopic data on xenoliths representing the mantle lithosphere are available for the Fernando de Noronha Island and only one locality, Pico Cabugi, in north-eastern Brazil and show consistently different isotopic arrays, trending from DM towards an EMII and an EMI component, respectively (Rivalenti et al., 2000). The effects of the Fernando de Noronha plume impingement on the continental lithosphere remains, therefore, at present largely unconstrained.

Thus, in order to better constrain the effect of the plume on the lithosphere in north-eastern Brazil and add further evidence on the processes which affected the continental mantle lithosphere, we provide in this paper new geochemical and isotope data on the xenoliths of four unstudied Brazilian localities. We will show that the lithosphere had a steep geothermal gradient and was geochemically heterogeneous. The higher temperature regions record Cenozoic, melt-assisted, near-fractional melting induced by infiltration of asthenospheric alkali basalts having EMI-like isotope characteristics. The colder lithospheric regions, composed of fertile protogranular spinel-lherzolites, have higher $^{143}Nd/^{144}Nd$ isotope values and geochemically record ancient mantle processes, probably related to the Mesozoic tholeiitic events. The transition between these two regions underwent percolation of small melt volumes, which produced chromatographic enrichment of highly incompatible elements and high $^{87}Sr/^{86}Sr$.

2. Analytical methods

Bulk-rock xenolith analyses were made on powders from cores only of samples having average diameters > 8 cm. These samples were cut into 1-cm thick slabs. Slabs were crushed to 2-mm size in a hardened steel mortar and 100 g of the sample thus obtained was ground in an agate mortar.

Major elements, Cr and Ni in bulk-rock xenoliths and basalts were analysed on glass discs at the Instituto de Geociências, University of São Paulo, according to Mori et al. (1999), using a Philips PW2400 XRF spectrometer. Sr, Y, Zr, Nb, Ba, REE, Hf, Ta, Th and U in bulk-rock powders were analysed by Inductively Coupled Plasma-Mass Spectrometry (ICP-MS) at the Department of Earth Sciences of the Memorial University of Newfoundland, St. John's, NF, Canada. Full details of the procedure are given in Jenner et al. (1990) and on the analytical accuracy in Rivalenti et al. (2004a). Trace elements in basalts were analysed by ICP-MS at the Instituto de Geociências, University of São Paulo. Samples were dissolved in Parr bombs in a microwave furnace. Accuracy, determined with respect to the reference standards BHVO-2 and BR, is 0.5–2%.

Modes were calculated using the PETMIX programme (available in the WEB site http://uni-geochem.gwdg.de/docs/binaries.htm) from the chemical composition of the minerals and bulk-rock according to LeMaitre (1979). In the absence of bulk-rock analyses, modes were estimated by point counting.

Major element, Ti and Cr mineral analyses were carried out on polished sections at the "Dipartimento di Scienze della Terra, Università di Modena e Reggio Emilia", Italy, with an ARL-SEMQ electron microprobe in wavelength dispersive mode, with an accelerating potential of 15 kV, a beam current of 20 nA, and a focused spot size of about 4 μm. Natural minerals were used as standards. Each element was counted 10 s, except for Ca in olivine, which was counted 40 s. Counts were converted to weight percent oxides using the PROBE software by J.J. Donovan (Advanced Microbeam 4217 C,

Authors Personal copy

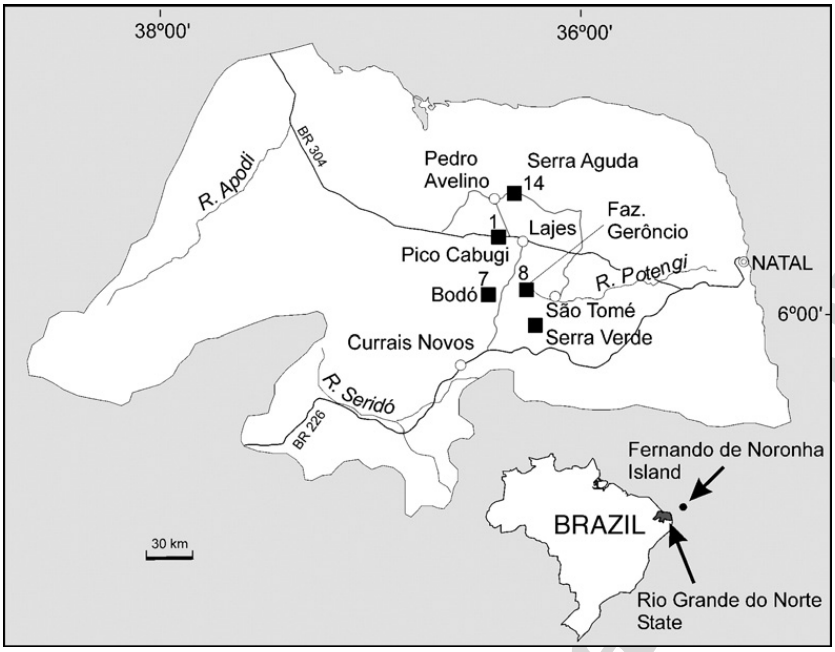

Fig. 1. Map of the sampled xenolith occurrences in north-eastern Brazil. New localities (black squares) are: Serra Aguda (AG, 5.30°S, 36.18°W), Bodó (BO, 5.58°S, 36.22°W), Fazenda Geroncio (GR, 5.58°S, 36.14°W) and Serra Verde (SV, 6.06°S, 36.12°W). Pico Cabugi was studied by Rivalenti et al. (2000). The numbers refer to the localities described by Fodor et al. (1998).

Kings Graces road, Vienna OH 44473 USA). Results are considered accurate within 2–6%.

Trace elements in clinopyroxene were analysed *in situ* by LA-ICP-MS at the "CNR-Istituto di Geoscienze e Georisorse, Section of Pavia", constituted by an Elan DRC-e mass spectrometer coupled with a Q-switched Nd:YAG laser source (Quantel Brilliant). The analytical method is described in detail in Rivalenti et al. (2004b).

Isotopic analyses in bulk-rock and clinopyroxene separates were carried out at Geochronological Research Center of the University of São Paulo, Brazil. The Rb–Sr and Sm–Nd analyses were prepared by standard methods described by Sato et al. (1995). Abundances of Rb and Sr were determined by isotope dilution using ^{87}Rb and ^{84}Sr enriched spikes. Due to the low Rb and Sr contents, blank corrections were required to final calculations. Each sample was ultrasonically washed in triple distilled water before chemical attack and all samples were totally digested with $HF_{(conc.)}$ plus $HNO_{3(conc.)}$ in a proportion 2:1, using Parr type bombs. The solutes were evaporated to dryness and converted to chloride form with 2.62 N HCl. Sr was separated in AG 50 WX8, 200–400 mesh cationic resin, loaded on Ta filaments together with 2 µl H_3PO_4 and analysed in the 262 Finnigan-Mat mass spectrometer. The Sr isotopic ratios were normalized to $^{86}Sr/^{88}Sr=0.1194$; replicate analyses of $^{87}Sr/^{86}Sr$ for the NBS987 standard gave a mean value of 0.71028± 0.00006 (2σ), the blanks for Sr were 5 ng.

Samples for Sm–Nd analyses were spiked with a ^{150}Nd–^{149}Sm spike and dissolved with $HF_{(conc.)}$ and $HNO_{3\ (conc.)}$ in proportion 2:1, also in Parr type bombs. The solutes were evaporated, converted with 0.2 ml 2.5 N HCl and the rare earth elements (REE) were separated with 6.2 N HCl in a AG 50WX8, 200–400 mesh cationic exchange resin. The solutions were dried and re-dissolved in 0.26 N HCl and Sm was collected with 0.55 N HCl. Both elements were loaded as phosphates on Re filaments and analysed in the 262 Finnigan-Mat mass spectrometer. Measurements of $^{143}Nd/^{144}Nd$ were normalized to $^{146}Nd/^{144}Nd=0.719$. The averages of $^{143}Nd/^{144}Nd$ for La Jolla and BCR-1 standards were 0.511847±0.00005 (2σ) and 0.512662±0.00005 (2σ), respectively. The blanks of Nd were less than 0.03 ng.

3. Xenolith description and petrography

Although most Tertiary alkali basalts in north-eastern Brazil contain small mantle xenoliths (Fodor et al., 1998), only four new localities have xenoliths exceeding 5 cm in diameter, suitable for study purposes. These localities (Fig. 1) have similar petrographic characteristics and are distinguished on the basis of the sample label (SA=Serra Aguda, BO=Bodò, GR=Fazenda Geroncio and SV=Serra Verde). Host lavas are alkali basalts and basanite, whose main petrographic and geochemical characteristics are reported in Fodor et al.

Author's personal copy

Table 1
Modal composition of the peridotite xenoliths

Sample	Group 1							Group 2					Group 3				
	AG6*	AG7^	BO9*	GR1^	SV2^	SV8*	SV14^	AG3*	AG4^	BO1^	BO15*	SV12^	AG1^	AG5^	AG8*	BO2^	BO11^
ol	63.8	75	60.7	73	76	70.8	65	60.5	60	60.8	70.9	65	65	69	58.8	70	65
cpx	13.2	4	11.5	3	8	7.0	35	10.2	15	14.8	12.1	3	8	10	16.0	4	8
opx	21.4	20	25.4	23	15	20.6	tr	27.3	23	22.0	14.5	30	25	20	21.8	25	25
sp	1.5	1	2.4	1	1	1.6	tr	2.1	2	2.5	2.5	2	2	1	3.4	1	2

*Calculated by combining mineral and bulk-rock analyses; ^ calculated by point counting; tr=trace.

(1998; new analyses in Supplementary Table 1, see Appendix A).

All the xenoliths are rounded (to angular at Serra Aguda) spinel-facies peridotites. Rivalenti et al. (2000) grouped the Pico Cabugi xenoliths in two textural types, porphyroclastic and protogranular (Mercier and Nicolas, 1975) and found they had different geochemical and petrological characteristics. This textural distinction applies also to the sample collection from the new localities.

Porphyroclastic xenoliths (*Group 1*, lherzolites AG6 and BO9, cpx-poor lherzolites SV2 and SV8, harzburgites GR1 and AG7 and wehrlite SV14, Table 1) are constituted by large porphyroclasts dominantly of olivine and more rarely orthopyroxene (size 1–9 mm) surrounded by a fine-grained (<1 mm) equigranular matrix of olivine, clinopyroxene and orthopyroxene having rectilinear grain boundaries and 120° triple junctions (Fig. 2A). The porphyroclastic orthopyroxene contains fine exsolution lamellae and porphyroclastic olivine is deformed. The matrix pyroxenes are always unexolved and clear.

Protogranular xenoliths (*Group 2*, lherzolites BO1, BO15, AG3 and AG4 and harzburgite SV12, Table 1) have curvilinear grain boundaries and olivine and pyroxenes grain size ranging 1–6 mm (Fig. 2B). Both clino- and orthopyroxene typically contain pyroxene exsolution lamellae. Spinel is an interstitial phase.

Personal copy

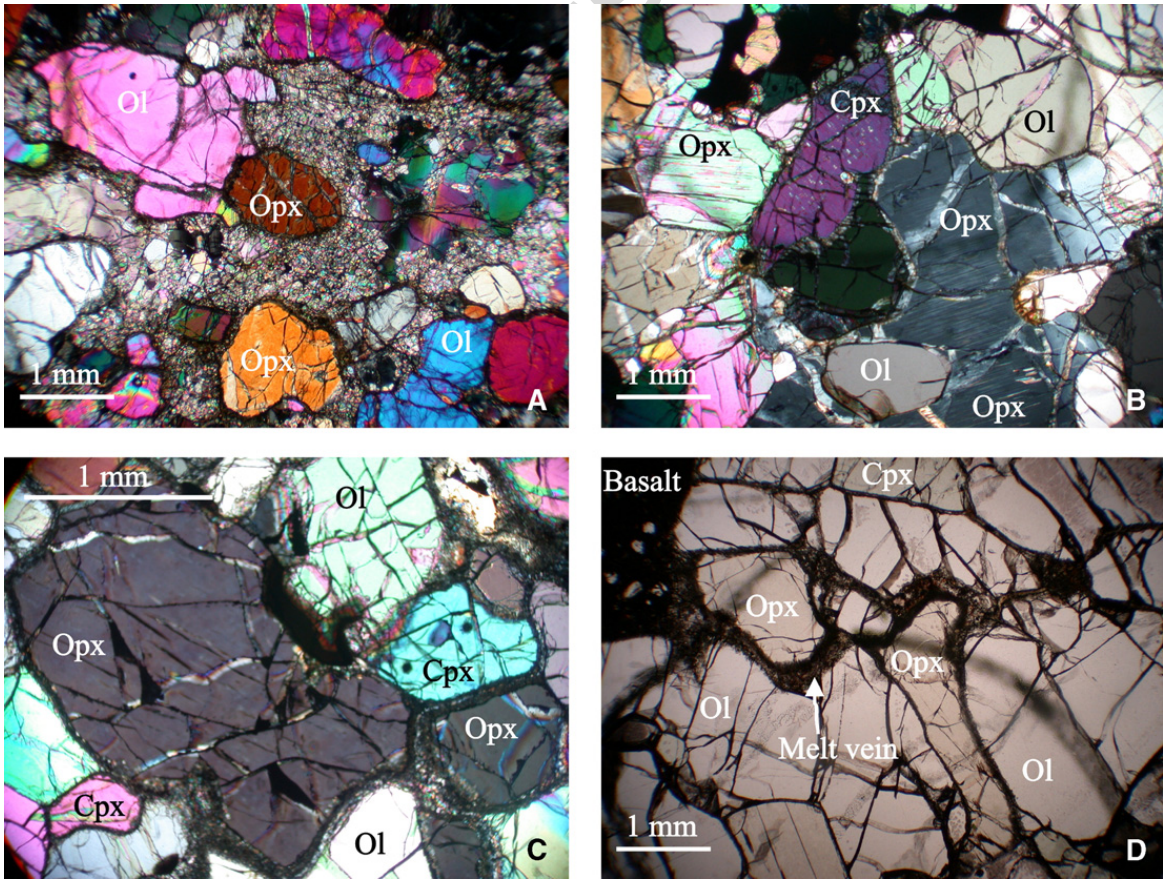

Fig. 2. A: Porphyroclastic texture in a *group 1* xenolith (AG6); B: protogranular texture in a *group 2* xenolith (AG3); C: texture in a *group 3* xenolith (AG8) showing exsolution lamellae only in orthopyroxene; D: melt vein infiltrated from the host basalt (SV2).

Other xenoliths (*Group 3*, lherzolite AG5 and AG8, cpx-poor lherzolites AG1 and BO11, and harzburgite BO2, Table 1) have characteristics transitional between *group 1* and *2*, although closer to the latter. They exhibit exsolution lamellae only in orthopyroxene, whereas clinopyroxene is an unexolved, clear phase or exhibits fine lamellae only in the crystal cores (Fig. 2C). Grain boundaries may be rectilinear (e.g. samples AG1 and BO11). All the samples contain small amounts of fine-grained (<1 mm) olivine and pyroxene veins or clusters.

Interstitial veins of altered glass, up to a few microns thick and often visible only by SEM, are common in most xenoliths and constitute <1% by volume of the rock. Samples BO2, AG6, AG7, SV2 and SV12 exhibit clear evidence that these veins originate at the basalt-xenolith edge and are, therefore, infiltration of basalt (Fig. 2D). The percolated melt reacted with the matrix pyroxenes and olivine. Secondary olivine, clinopyroxene and spinel (~ 0.1 mm in diameter) were the reaction products.

4. Analytical results

4.1. Bulk-rock

Only seven xenoliths from the new localities had dimensions suitable for bulk analysis (Supplementary Table 2, Appendix A). Simple mass balance calculation shows that the presence of <1% by volume infiltrated basalt has a negligible effect on the peridotite major element concentration, while it may greatly influence that of incompatible minor and trace elements, as well as their isotopic composition. For this reason, only major elements are here considered, whereas complete analyses, including isotopes, are stored in Supplementary Table 2 (Appendix A) for reader's information.

Incompatible major element concentrations and modal clinopyroxene decrease as the MgO increases (Fig. 3), as previously described and discussed for the Pico Cabugi and Fernando de Noronha xenoliths by Rivalenti et al. (2000). The major element variation array of the *group 1* xenoliths overlaps that of the other groups, but, together with the Pico Cabugi and Fernando de Noronha porphyroclastic samples, it contains the MgO-richer peridotites. Compared with the field of the abyssal peridotites (Baker and Beckett, 1999), the present xenoliths have, at a given MgO concentration, lower SiO_2, Al_2O_3, CaO and FeO, and higher TiO_2, concentrations and behave, in this respect, as the ultramafic nodules and peridotite massifs reported for comparison by Baker and Beckett (1999). The present xenoliths also contain higher TiO_2 and lower SiO_2, Al_2O_3, CaO with respect to the model melting-related depletion trends of Niu (1997) for oceanic mantle (Fig. 3).

4.2. Clinopyroxene

Crystal core analyses are reported in Table 2 and the rim analyses in Supplementary Table 3, see Appendix A. The Mg# values [$100 \times Mg/(Mg+Fe_{tot})$, molar] largely overlap in the three groups and range 87.9–92.3, 90.2–92.1 and 89.4–91.3 in *groups 1*, *2* and *3*, respectively. When major elements (in a.f.u.) are plotted against the Mg# variation, the *group 1* clinopyroxenes have, at any given Mg# value, lower concentrations of Ti, Al, Ca and Na with respect to *group 2*. In the Ti and Al diagrams, *group 3* defines an array intermediate between *groups 1* and *2* (Fig. 4). The *group 1* clinopyroxenes also are the richest in Fe (and obviously in MgO wt.%, in order to maintain a similar Mg# range with the other groups) and *group 3* clinopyroxenes are Fe-richer than those of *group 2*. When compared with the Pico Cabugi and Fernando de Noronha data (Rivalenti et al., 2000), the *group 1* variation trends parallel or overlap those observed in the clinopyroxenes of the porphyroclastic xenoliths, and the composition of the *groups 2* and *3* clinopyroxenes are similar to those of the protogranular ones (Fig. 4).

Most of clinopyroxenes are zoned. Compositional variation affects the outer, 3–4 μm large, rim and is negligible with respect to the variation from one sample to the other (Supplementary Table 3, Appendix A, and Fig. 4). The rims of most *group 2* clinopyroxenes trend toward the composition of more pure diopside with respect to the core, except for Ti that increases rimwards (Fig. 4). In *group 1* the rims are somewhat more fertile (richer in Ti, Al, Ca and Na) and in *group 3* Ti and Al decrease, Mg# increases and Na variation is negligible (Supplementary Table 3, Appendix A, and Fig. 4).

Incompatible trace element concentrations of the clinopyroxene cores are reported in Table 2 and illustrated in Fig. 5 as Primitive Mantle (PM)-normalised REE and multielement patterns (PM concentrations by Hofmann, 1988). The *group 1* REE patterns mainly vary from L-MREE-enriched convex-upward ($La_n/Sm_n = 0.49–0.52$; $Sm_n/Yb_n = 1.99–2.85$; samples AG6, AG7 and GR1 in Fig. 5A) to spoon-shaped (BO9 and SV2; $La_n/Nd_n = 2.2–5.7$; $Nd_n/Yb_n = 0.2–1.03$; Fig. 5B). SV8 clinopyroxene is characterised by a strong fractionation in the M-HREE region (also displayed by clinopyroxene BO9) and a significant depletion in LREE ($La_n = 0.3$). The latter is enriched with respect to Ce ($La_n/Ce_n = 1.3$), which suggests a possible incipient development of spoon-shaped fractionation. Clinopyroxene from wehrlite SV14 has a

Author's personal copy

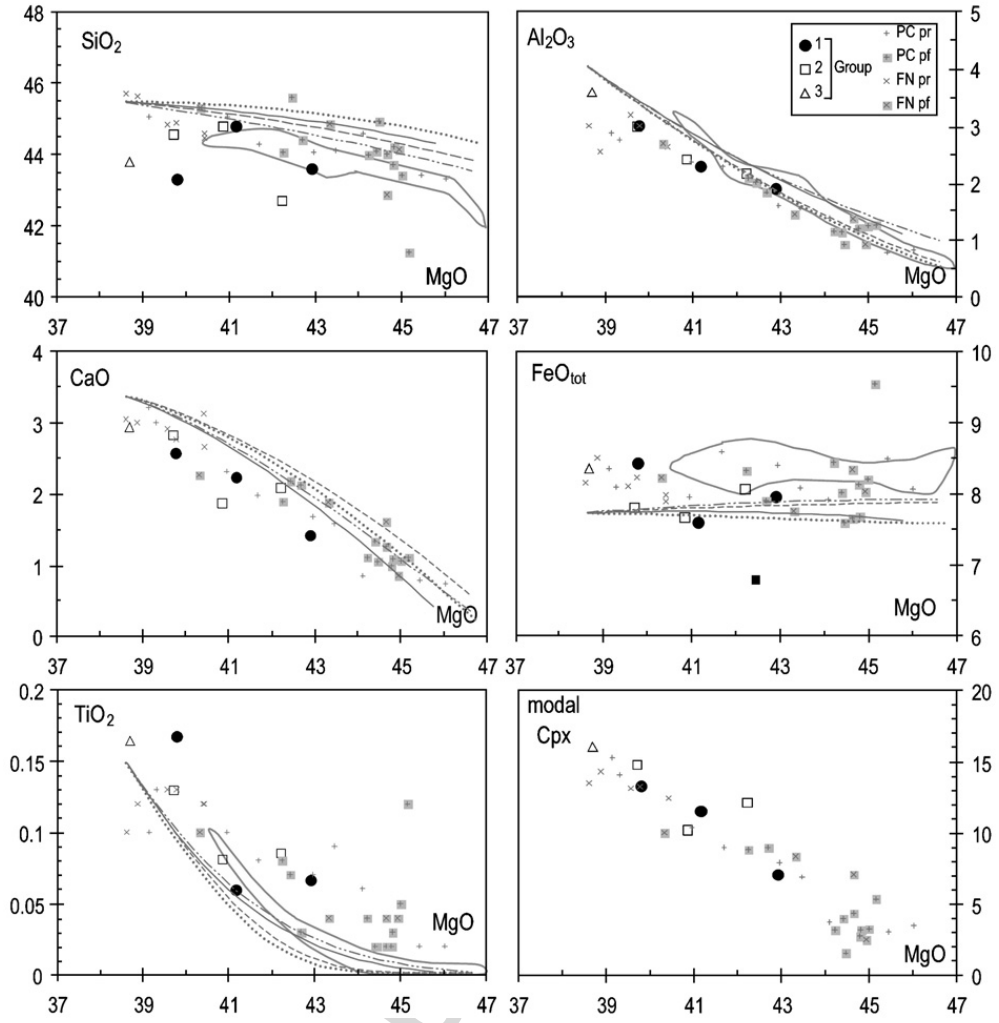

Fig. 3. Bulk-rock variation of major elements (wt.%) and modal clinopyroxene with respect to MgO (wt.%). The lines are model peridotite residues up to ~ 25% melting from batch (black line, 2 GPa; dash-dots line, 1 GPa) and polybaric fractional melting (dotted line, 2.5–0.8 GPa; dashed line, 1.5–0.8 GPa) from Niu (1997). Contoured field: abyssal peridotites (Baker and Beckett, 1999). The Pico Cabugi (PC) and Fernando de Noronha (FN) xenoliths (Rivalenti et al., 2000) are plotted in grey (pf=porphyroclastic; pr=protogranular).

LREE-enriched, steadily fractionated, REE pattern (Ce_n/Yb_n=10.8; Fig. 5B).

The convex-upward clinopyroxenes have the lowest Mg# values (87.9–90.1) and the spoon-shaped clinopyroxenes the highest (92.0–92.3), with Mg# equal to 91.3 and 91.4 in clinopyroxenes from SV8 and SV14, respectively (Fig. 5A).

Th and U are enriched with respect to Nb in the spoon-shaped clinopyroxenes (Th_n/Nb_n=1.3–8.4), which also show a positive Sr spike. The latter feature is also shown by clinopyroxene GR1 and SV14. Nb content is very variable (in the range 0.2–3 ×PM), with La_n/Nb_n=1.0–5.7. All the clinopyroxenes show negative Zr, Hf and Ti anomalies. The highest negative HFSE anomalies occur in clinopyroxene SV14 (Zr_n/Zr^*_n=0.1; Hf_n/Hf^*_n=0.09; Ti_n/Ti^*_n=0.42; where $HFSE_n/HFSE^*_n=HFSE_n/[10^{(\Sigma\log \text{adjacent } REE_n/2)}]$. With respect to the other groups, the convex-upward *group 1* clinopyroxenes have lower Dy to Yb and HFSE concentrations and the spoon-shaped clinopyroxenes are the poorest in REE (except La), Zr, Hf and Ti.

The *group 2* clinopyroxenes are predominately LREE-depleted and flat to slightly HREE enriched from M- to HREE (La_n/Nd_n=0.34–0.48; Nd_n/Yb_n=0.71–1.04) (Fig. 5C). An exception is BO1, slightly LREE enriched and steadily fractionated (Ce_n/Yb_n=1.27). All the clinopyroxenes are U and Th enriched with respect to Nb, but not with respect to LREE. Nb is constantly depleted with respect to La (La_n/Nb_n=3.4–19.2). HFSE anomalies are modest (Zr_n/Zr^*_n=0.67–0.84; Hf_n/Hf^*_n=0.58–0.97; Ti_n/Ti^*_n=0.66–0.77).

The *group 3* clinopyroxenes have M-HREE concentrations and profiles similar to those of *group 2*, but most have higher LREE concentrations (La_n/Nd_n=

Table 2
Major (wt%) and trace (ppm) element core concentration, Sr and Nd isotopes in Clinopyroxene and temperature (°C), pressure (GPa) estimates

	GROUP 1							GROUP 2					GROUP 3				
Sample	AG6c	AG7c	BO9c	GR1c	SV2c	SV8c	SV14c	AG3c	AG4c	BO1c	BO15c	SV12c	AG1c	AG5c	AG8c	BO2c	BO11c
Lithotype	Lh	Ha	Lh	Ha	Lh	Lh	We	Lh	Lh	Lh	Lh	Ha	Lh	Lh	Lh	Ha	Lh
SiO_2	50.02	52.72	52.64	52.20	53.16	52.47	52.43	51.85	52.17	52.33	52.39	52.64	52.29	51.44	51.32	52.81	52.22
TiO_2	0.65	0.48	0.15	0.32	0.14	0.23	0.18	0.52	0.72	0.61	0.55	0.66	0.42	0.76	0.70	0.47	0.42
Al_2O_3	7.73	5.12	5.00	6.22	3.79	5.82	4.19	6.14	7.00	7.17	6.16	6.25	6.13	8.32	7.11	6.16	6.37
Cr_2O_3	0.82	1.71	0.92	1.56	0.77	0.92	1.43	0.88	0.58	0.84	0.94	0.86	0.77	0.22	0.72	0.96	0.74
FeO_{tot}	4.25	3.77	2.50	3.53	2.47	2.74	2.73	2.23	2.84	2.38	2.38	2.36	2.80	3.04	2.79	2.49	2.78
MnO	0.17	0.11	0.09	0.11	0.06	0.08	0.08	0.09	0.10	0.08	0.08	0.06	0.05	0.10	0.08	0.06	0.09
NiO	0.03	0.08	0.09	0.04	0.06	0.06	0.05	0.04	0.04	0.06	0.03	0.04	0.04	0.04	0.03	0.05	0.09
MgO	17.25	18.68	16.11	17.94	16.71	16.06	16.28	14.49	14.67	14.41	14.67	14.89	15.20	14.39	14.56	14.75	14.82
CaO	17.58	16.51	21.34	17.94	21.69	20.42	19.60	20.77	19.95	20.49	19.64	20.79	21.06	20.37	20.01	20.43	19.55
Na_2O	1.12	1.16	1.19	1.18	0.71	1.29	1.39	1.86	2.04	2.11	1.89	1.89	1.67	1.90	2.09	1.97	2.06
Total	99.61	100.34	100.02	101.03	99.55	100.08	98.36	98.87	100.11	100.47	98.73	100.43	100.43	100.58	99.40	100.15	99.13
Mg#	87.87	89.84	91.99	90.07	92.33	91.27	91.40	92.06	90.21	91.51	91.66	91.85	90.64	89.40	90.28	91.33	90.49
Sc	32.5	36.4	53.4	40.3	49.2	47.7	51.7	59.8	55.9	53.5	55.4	60.4	55.3	44.0	54.9	54.9	54.8
Rb			0.14	0.16	0.037	0.32	0.076	0.014	0.014	0.045	0.086	0.31	0.24	1.20	0.18	0.014	0.022
Sr	56.0	65.1	16.7	91.3	38.9	9.4	159.7	56.0	77.0	119.2	65.0	64.2	59.6	74.2	82.2	56.1	122.3
Y	10.0	9.2	7.3	4.3	4.9	9.5	4.9	14.2	17.0	14.7	14.1	15.4	12.5	10.7	15.1	12.3	12.8
Zr	14.7	15.0	2.01	8.1	4.0	4.2	4.6	21.0	35.4	32.9	22.5	29.7	17.7	21.9	29.1	17.6	13.6
Nb	0.22	0.24	0.68	0.26	1.03	0.13	2.19	0.078	0.051	0.88	0.13	0.13	0.022	0.22	0.066	0.25	0.11
Ba	0.084	0.16	0.19	2.69	0.59	0.38	0.10		0.19	0.77	0.05	0.43	0.064	0.16	0.25	0.086	0.12
La	1.25	1.37	0.66	0.76	5.1	0.19	4.6	0.58	0.97	2.93	0.89	0.77	4.3	1.69	1.07	0.69	6.92
Ce	5.4	4.9	0.84	2.66	4.7	0.41	12.6	2.54	4.1	9.0	3.6	3.4	5.9	5.9	4.1	2.52	13.3
Pr	0.88	0.86	0.11	0.48	0.38	0.10	1.55	0.51	0.79	1.14	0.62	0.62	0.57	0.93	0.70	0.46	1.16
Nd	4.5	4.7	0.58	2.58	1.74	0.72	7.04	3.3	4.6	6.0	3.6	3.7	2.95	5.0	4.2	2.82	4.2
Sm	1.62	1.64	0.34	0.98	0.60	0.60	1.42	1.27	2.11	1.97	1.40	1.60	1.15	1.70	1.69	1.23	1.31
Eu	0.64	0.59	0.16	0.37	0.22	0.26	0.53	0.59	0.77	0.88	0.67	0.71	0.54	0.69	0.76	0.51	0.54
Gd	1.78	1.82	0.78	0.92	0.72	0.96	1.21	1.78	2.46	2.36	1.94	2.02	1.56	1.86	2.06	1.63	1.65
Tb	0.31	0.31	0.15	0.16	0.11	0.23	0.17	0.36	0.46	0.42	0.36	0.42	0.33	0.31	0.42	0.31	0.34
Dy	1.89	1.76	1.31	0.88	0.83	1.64	0.99	2.71	3.2	2.75	2.62	2.72	2.29	2.07	2.83	2.21	2.35
Ho	0.39	0.36	0.25	0.19	0.21	0.38	0.18	0.56	0.69	0.61	0.57	0.57	0.50	0.42	0.66	0.50	0.53
Er	0.99	0.82	0.90	0.41	0.53	1.00	0.44	1.45	1.86	1.70	1.49	1.84	1.31	1.20	1.77	1.35	1.47
Tm	0.13	0.12	0.13	0.06	0.08	0.15	0.055	0.23	0.28	0.24	0.19	0.24	0.18	0.16	0.25	0.19	0.21
Yb	0.88	0.76	0.99	0.37	0.59	1.15	0.30	1.52	1.90	1.84	1.41	1.81	1.45	1.27	1.91	1.58	1.50
Lu	0.10	0.10	0.13	0.056	0.078	0.16	0.046	0.21	0.27	0.23	0.20	0.26	0.19	0.14	0.24	0.18	0.20
Hf	0.67	0.64	0.10	0.34	0.15	0.25	0.12	0.71	1.15	0.79	0.66	0.94	0.60	0.68	0.96	0.53	0.45
Ta	0.030	0.024	0.022	0.020	0.020	0.009	0.29	0.008	0.009	0.067	0.017	0.043		0.029	0.020	0.019	0.007
Th	0.029	0.030	0.11	0.028	1.14	0.015	0.33	0.011	0.021	0.18	0.016	0.011	0.94	0.073	0.026	0.013	2.36
U	0.008	0.007	0.065	0.009	0.21		0.80	0.006	0.007	0.079	0.11	0.006	0.24	0.018	0.010	0.022	0.68
Sm ID				1.883	0.777		1.954		2.110			1.702	1.334	2.023		1.529	1.874
Nd ID				6.420	2.928		8.307		5.219			4.863	3.134	5.466		3.655	6.790
$^{87}Sr/^{86}Sr$				0.70407	0.70366		0.70313		0.70248			0.70380	0.70387	0.70329		0.70233	0.70388
Error				0.00011	0.00018		0.00019		0.00016			0.00014	0.00021	0.00022		0.00016	0.00012
$^{147}Sm/^{144}Nd$				0.1773	0.1606		0.1423		0.2444			0.2116	0.2574	0.2238		0.2529	0.1669
Error				0.0007	0.0006		0.0005		0.0008			0.0007	0.0009	0.0008		0.0009	0.0006
$^{143}Nd/^{144}Nd$				0.512676	0.512743		0.512876		0.513079			0.512954	0.513391	0.513064		0.513336	0.513121
Error				0.000036	0.000063		0.000014		0.000011			0.000008	0.000012	0.000010		0.000012	0.000013
T_{BK}	1217	1280	953	1221	992	1045	1095	827	951	872	994	890	889	935	904	909	977
P_M	2.3	2.6	1.8	2.3	2.0	1.9	2.1	1.3	1.8	1.4	1.8	1.5	1.6	1.5	1.7	1.6	2.0
P_{KB}	1.5	2.4	1.6	2.0	1.9	1.0		0.6	2.1	1.3	2.9	1.3	0.7		0.3	1.8	1.9

ID=Isotope dilution analysis, Error=2σ. T_{BK}=Geothermometer of Brey and Köhler (1990) at 1.6 Gpa. P_M=Geobarometer of Mercier et al. (1984). P_{KB}=Geobarometer of Köhler and Brey (1990).

Author's personal copy

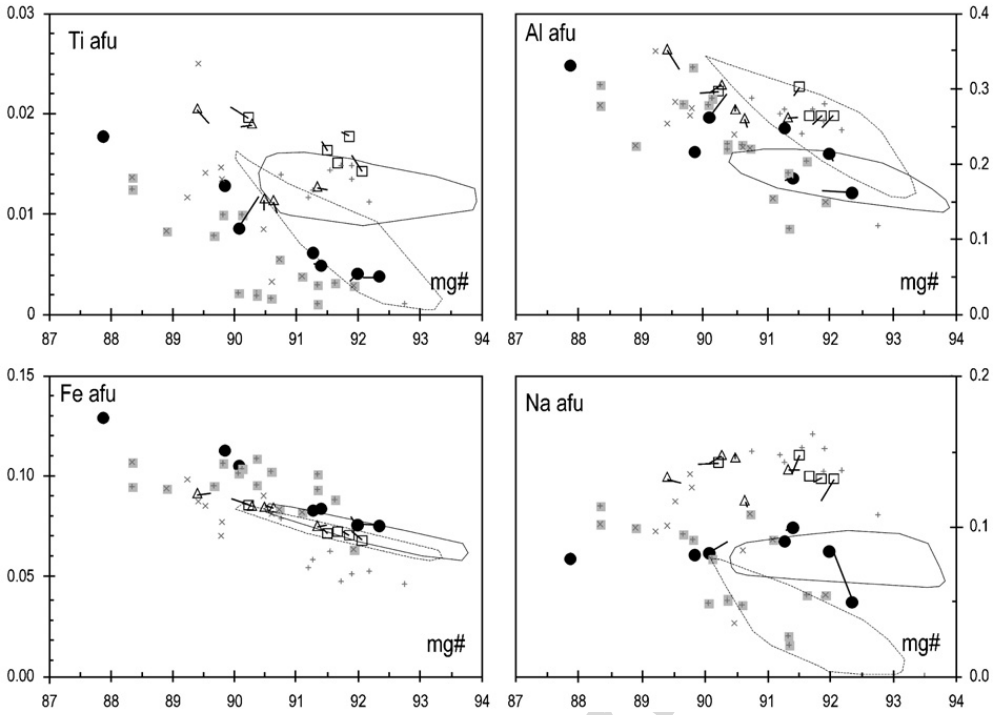

Fig. 4. Variation of Ti, Al, Ca and Na (a.f.u.) with respect to Mg# in clinopyroxene. Tails connect core (the symbol) and rim (end of the tail) composition. Symbols as in Fig. 3. Pico Cabugi and Fernando de Noronha samples (Rivalenti et al., 2000) are plotted in grey (pf=porphyroclastic; pr=protogranular). The continuous line contours the clinopyroxenes of continental peridotite massifs from Western Alps (Rivalenti and Mazzucchelli, 2000) and the dashed line that in abyssal peridotites (Johnson et al., 1990; Johnson and Dick, 1992). The first resemble the *groups 2* and *3* clinopyroxenes, and the second resemble *group 1*.

0.48–0.65). Two samples (AG1 and BO11) have spoon-shaped, LREE-enriched profiles (La_n/Nd_n=2.85–3.19) and Nd to Yb concentrations within the range of the other *group 3* samples (Fig. 5D). These two samples have also the highest Th and U concentrations with respect to Nb (Th_n/Nb_n=161 and 327 in AG1 and BO11, respectively and 0.40–3.03 in the other *group 3* clinopyroxenes).

4.3. Orthopyroxene

The Mg# values range 89.2–91.3, 89.3–90.9, 88.9–90.8 in *groups 1*, *2* and *3*, respectively (crystal core analyses reported in Table 3; rim analyses in Supplementary Table 4, Appendix A). At any given Mg# value the *group 1* orthopyroxenes have higher Ti, Al, Ca, Na and lower Fe with respect to those of the other groups and *group 3* has concentrations intermediate between *groups 1* and *2* (Table 3, Figure not shown). These differences are the opposite of those observed in clinopyroxene and are obviously reflected in different cpx/opx element distribution between the three groups, as illustrated for Ti, Al, Ca and Na in Fig. 6. Rimward variations occur and are similar to those observed in clinopyroxene, so that the orthopyroxene rims in *group 1* are richer, and in *groups 2* and *3* are poorer, in Ti and Al with respect to their respective cores.

4.4. Olivine and spinel

The olivine composition (Fo=88.4–90.7, Supplementary Table 5, Appendix A) is similar in three groups, but olivines of *group 1* have higher CaO concentrations (0.04–0.18 wt.%) than those of *group 3* (0.03–0.06 wt.%) and *group 2* (0.02–0.04 wt.%). The rims of *group 1* olivine have in general lower Fo and NiO and higher CaO than the respective cores, whereas in most *groups 2* and *3* olivines Fo concentration increases rimward and CaO and NiO remain constant or decrease.

Spinel exhibits a Cr# vs. Mg# (Cr#=[Cr/(Cr+Al+Fe^{3+}) a.f.u.] and Mg# [=Mg/(Mg+Fe^{2+}) a.f.u.]) variation trend (Supplementary Table 6 and Supplementary Figure, see Appendix A) similar to that of abyssal peridotites (Hellebrand et al., 2002). The *group 1* spinels have higher TiO_2 concentrations than the others (Supplementary Table 6, see Appendix A). In all groups the Cr# values increase with increasing Fo in the coexisting olivine, but *group 1* has Cr#-richer spinels

Author's personal

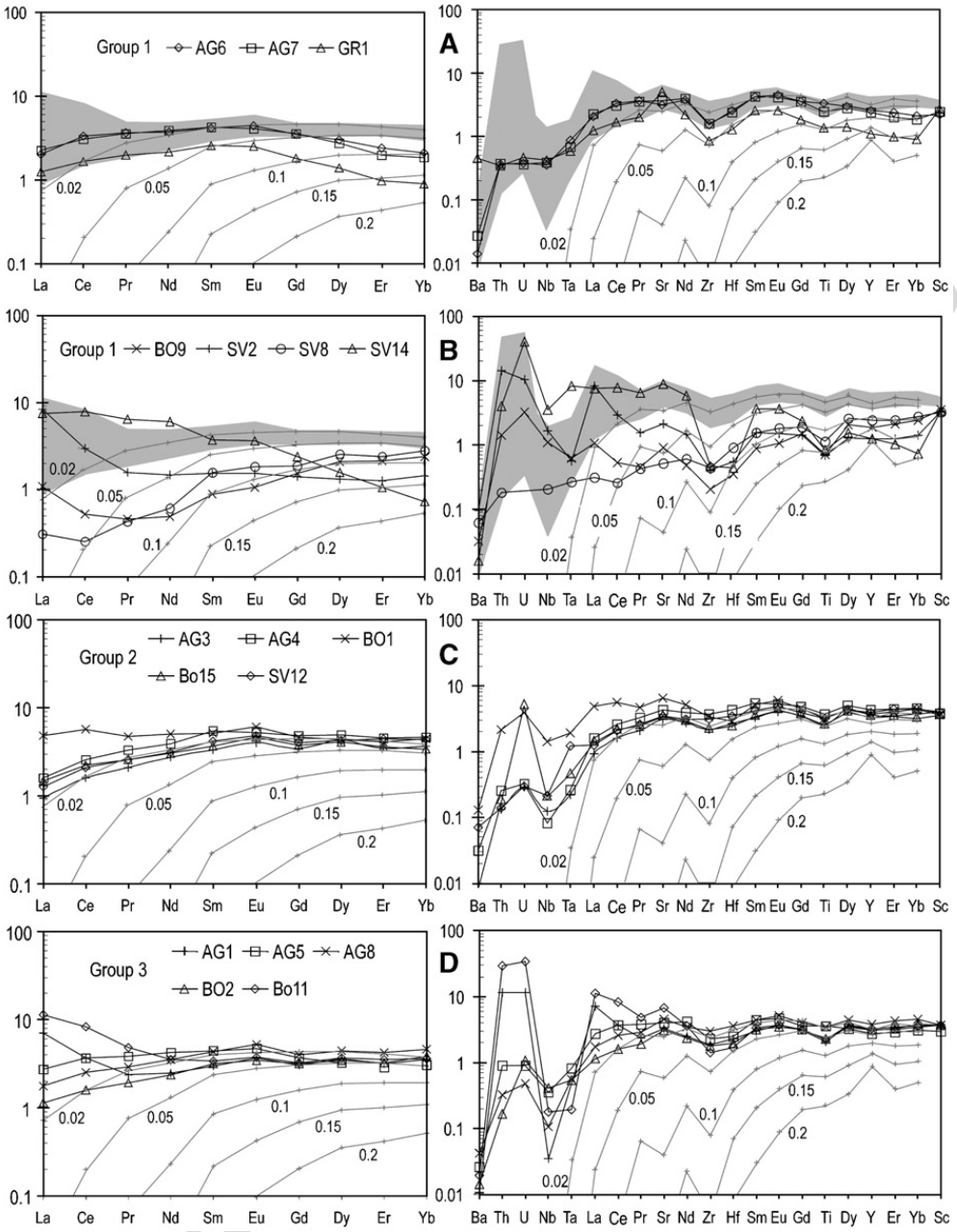

Fig. 5. Primitive Mantle (Hofmann, 1988) normalized REE and extended incompatible trace element patterns of clinopyroxenes. A: *group 1* clinopyroxenes having a convex-upward REE pattern; B: *group 1* clinopyroxenes having spoon-shaped (SV2 and BO9), LREE-depleted (SV8) and LREE-enriched, steadily fractionated (SV14) REE patterns; C: *group 2* clinopyroxenes; D: *group 3* clinopyroxenes. Model patterns of 2–20% fractional melting residua, calculated using the partition coefficients of Hart and Dunn (1993) and those reported in Rivalenti et al. (2004b) are shown in all the diagrams. The grey field reported for comparison in the A and B diagrams is that of the *groups 2* and *3* clinopyroxenes.

at a given Fo concentration in olivine (Supplementary Figure in the journal website).

4.5. Sr–Nd isotopes

The analytical results on clinopyroxene separates (Table 2) are illustrated in Fig. 7, along with the previous Pico Cabugi and Fernando de Noronha data (Rivalenti et al., 2000). Clinopyroxene compositions show a large scatter between the Bulk Earth (BE) value and a high Nd, very variable Sr, field that comprises DM. Within the isotope field, the present *group 1* clinopyroxenes (GR1, SV2 and SV14) have the lowest $^{143}Nd/^{144}Nd$ values and, together with porphyroclastic clinopyroxenes from Fernando de Noronha (FN6) and Pico Cabugi (Pc 109, Pc126 and Pc 135; Rivalenti et al., 2000),

Table 3
Major (wt%) element core concentration in Orthopyroxene

	Group 1						Group 2					Group 3				
Sample	AG6c	AG7c	BO9c	GR1c	SV2c	SV8c	AG3c	AG4c	BO1c	BO15c	SV12c	AG1c	AG5c	AG8c	BO2c	BO11c
Lithotype	Lh	Ha	Lh	Ha	Lh	We	Lh	Lh	Lh	Lh	Ha	Lh	Lh	Lh	Ha	Lh
SiO_2	52.04	55.17	55.34	54.14	56.39	55.61	55.89	55.28	55.22	55.53	55.56	55.83	54.99	54.97	55.14	55.05
TiO_2	0.27	0.19	0.04	0.12	0.05	0.09	0.10	0.13	0.11	0.12	0.13	0.09	0.13	0.14	0.09	0.08
Al_2O_3	6.23	3.88	3.65	4.94	3.49	4.84	3.80	4.17	3.90	3.67	3.94	4.24	5.13	4.32	3.64	4.05
Cr_2O_3	0.55	1.04	0.36	0.96	0.48	0.53	0.38	0.22	0.27	0.35	0.33	0.34	0.09	0.29	0.32	0.28
FeO_{tot}	6.49	5.63	5.86	6.00	5.99	5.76	6.12	6.99	6.28	6.24	6.25	5.99	7.02	6.61	6.18	6.26
MnO	0.16	0.11	0.15	0.13	0.14	0.12	0.13	0.16	0.14	0.15	0.15	0.14	0.17	0.17	0.16	0.15
NiO	0.11	0.13	0.11	0.13	0.10	0.14	0.10	0.11	0.11	0.09	0.10	0.13	0.11	0.11	0.04	0.10
MgO	30.22	32.45	33.85	31.63	33.23	32.56	33.50	32.84	33.69	33.87	34.24	32.83	32.36	32.90	33.98	32.47
CaO	1.56	1.79	0.56	1.52	0.66	0.95	0.54	0.47	0.43	0.43	0.36	0.64	0.57	0.54	0.46	0.54
Na_2O	0.16	0.18	0.04	0.15	0.03	0.11	0.05	0.09	0.06	0.04	0.05	0.10	0.10	0.11	0.05	0.12
Total	97.81	100.57	99.97	99.72	100.58	100.71	100.61	100.47	100.19	100.49	101.12	100.34	100.68	100.16	100.05	99.09
Mg#	89.24	91.13	91.15	90.39	90.82	90.97	90.71	89.33	90.54	90.63	90.71	90.72	89.15	89.87	90.74	90.24

define an elongated field (labelled *array 1* for simplicity) between DM and an enriched, EMI-like, component. The host basalts also record mixing between DM and EMI (Fodor et al., 1998), but, at a given $^{143}Nd/^{144}Nd$, they are higher in $^{87}Sr/^{86}Sr$, with respect to *array 1*.

Groups 2 and *3* clinopyroxenes have, at a given Sr isotopic value, much higher Nd isotopic values than those in *group 1* (Table 3 and Fig. 7). Within these groups, clinopyroxenes with LREE-depleted patterns are also isotopically different from those of *group 3* having LREE-enriched, spoon-shaped patterns. The first ones form an elongated field (*array 2*, Fig. 7) originating from DM and diverging from *array 1* for systematically higher $^{87}Sr/^{86}Sr$ at decreasing $^{143}Nd/^{144}Nd$. The porphyroclastic sample FN5 from Fernando de Noronha also plots in this array. The LREE-enriched, spoon-shaped clinopyroxenes, together with those from Fernando de Noronha protogranular peridotites (Rivalenti et al., 2000), outline a third isotopic field (*array 3*, Fig. 7) at high $^{87}Sr/^{86}Sr$ and $^{143}Nd/^{144}Nd$.

personal copy

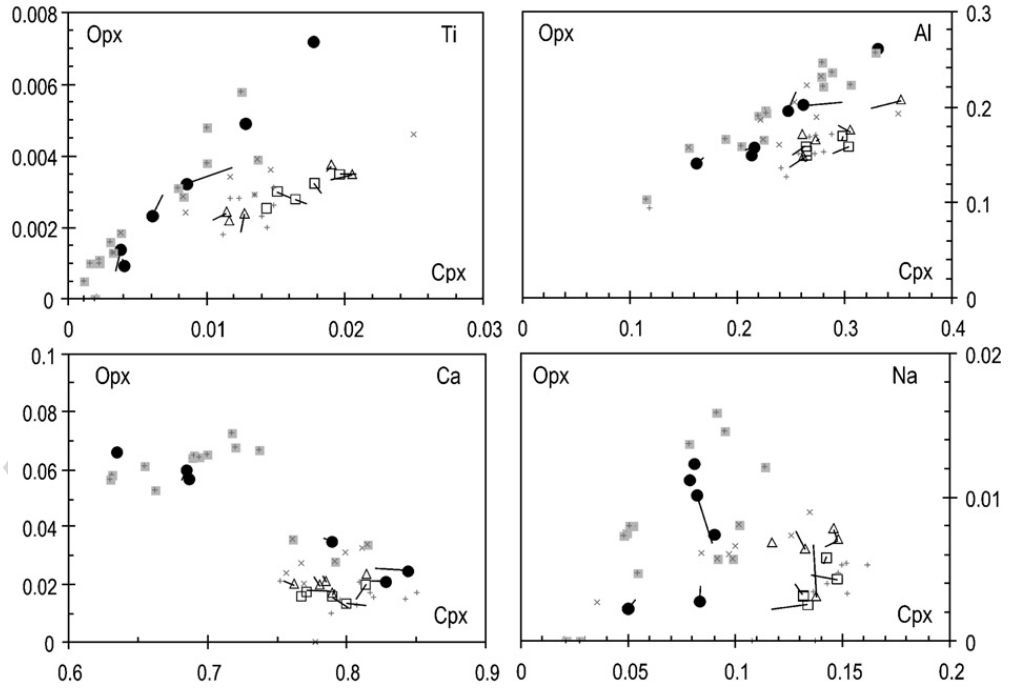

Fig. 6. Distribution of Ti, Al, Ca and Na (a.f.u.) between clino- and orthopyroxene. Tails connect core (the symbol) and rim (end of the tail) compositions. Pico Cabugi and Fernando de Noronha samples (Rivalenti et al., 2000) are plotted in grey. Symbols as in Fig. 3.

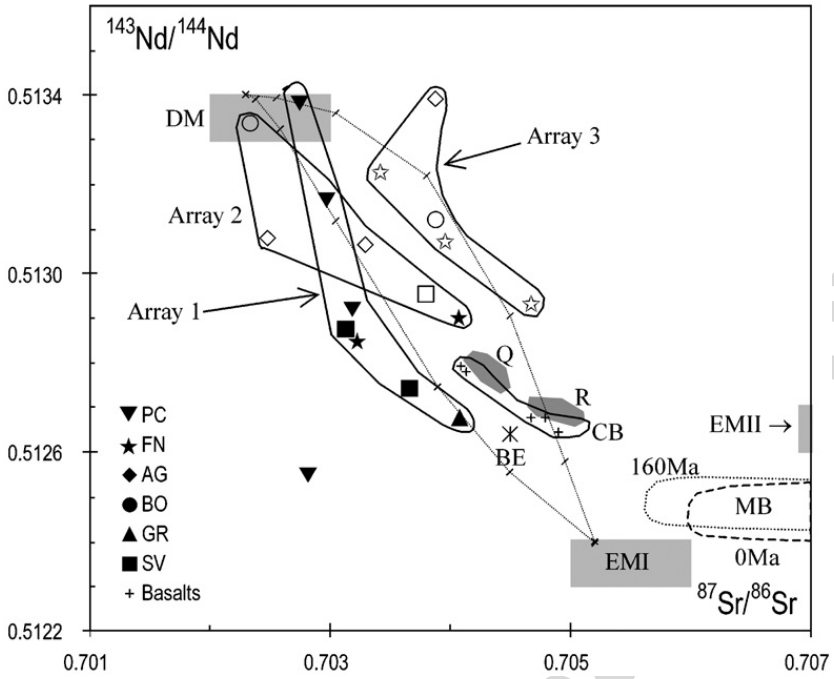

Fig. 7. Present-day $^{87}Sr/^{86}Sr$–$^{143}Nd/^{144}Nd$ diagram for clinopyroxenes, including those from Pico Cabugi and Fernando de Noronha (Rivalenti et al., 2000). Black symbols: porphyroclastic (*group 1*) xenoliths; open symbols: protogranular (*groups 2* and *3*) xenoliths. The fields labelled "*arrays 1*, *2* and *3*" correspond with the clinopyroxenes from porphyroclastic xenoliths (present *group 1*), the protogranular LREE-depleted clinopyroxenes (*groups 2* and *3*) and with the protogranular spoon-shaped clinopyroxenes (*group 3* and Fernando de Noronha), respectively. CB and MB indicate the fields of the Cenozoic (Fodor et al., 1998 and new data from Supplementary Table 1, Appendix A, as crosses) and Mesozoic (Fodor et al., 1990, present day values and recalculated at 160 Ma) basalts from north-east Brazil, respectively; Q and R: isotope fields of the Fernando de Noronha Quixaba and Remedios Formations, respectively (Gerlach et al., 1987). Fields of mantle end members from Faure (2001, p.58); BE: Bulk Earth. Thin lines are an AFC model discussed in the text. Ticks are 10% F steps. Parameters used in the model: $^{143}Nd/^{144}Nd$=0.5134 and 0.5124,$^{87}Sr/^{86}Sr$=0.7023 and 0.7052 in the peridotite and contaminant, respectively; bulk $^{solid/melt}D_{Sr}$=0.079, $^{solid/melt}D_{Nd}$=0.116; low porosity has been simulated by assuming R=0.99 (peridotite mass/contaminant mass); Peridotite: Sr=6, Nd=0.4. Basalt: Sr=115 and 1000, Nd=11 and 27, in concave-upward and convex-upward variation curve, respectively.

The Pico Cabugi clinopyroxene with the lowest $^{87}Sr/^{86}Sr$ and $^{143}Nd/^{144}Nd$ values (Pc 105), considered as an evidence of an EMI component by Rivalenti et al. (2000), plots well apart from the isotope range defined by the other xenoliths from north-eastern Brazil, suggesting further complexities in terms of geochemical reservoirs.

5. Temperature and pressure

Equilibrium temperatures of the xenoliths were calculated according to Brey and Köhler (1990), with the exception of wehrlite SV14, for which equilibrium temperature was estimated according to the single clinoproxene geothermometer of Mercier et al. (1984). As for pressure, there is no reliable geobarometer for spinel-facies peridotites, except perhaps the Ca-in-olivine geobarometer of Köhler and Brey (1990). This latter, however, requires high precision estimates of the Ca concentration in olivine (that we are not sure to have reached by increasing the microprobe counting time to 40 s for Ca) and is, anyway, not applicable below 900 °C (Yang et al., 1998). Although aware of its limits, we have used the empirical geobarometer of Mercier et al. (1984), as done by Yang et al. (1998), who discuss in detail the reasons justifying its use. It results that for most samples with equilibrium temperature>900 °C, the pressure estimated according to Köhler and Brey and to Mercier agree within ±0.3 GPa (Table 3).

The estimated T and P are reported in Table 2. The *group 1* xenoliths have higher T and P values than *group 2* (950–1280 °C, 1.9–2.5 GPa and 830–990 °C, 1.3–1.8 GPa, respectively), suggesting that *group 1* xenoliths represent a deeper lithospheric level. *Group 3* xenoliths have T and P values (890–980 °C, 1.5–2 GPa) intermediate between *groups 1* and *2*. The temperature–pressure variation (Fig. 8) is consistent with a thermal gradient of ~ 15 °C/km, which agrees with the results of Fodor et al. (2002). The temperature values recorded by the pyroxene rims in *group 2* are lower than those of the respective cores, whereas in

Author's personal copy

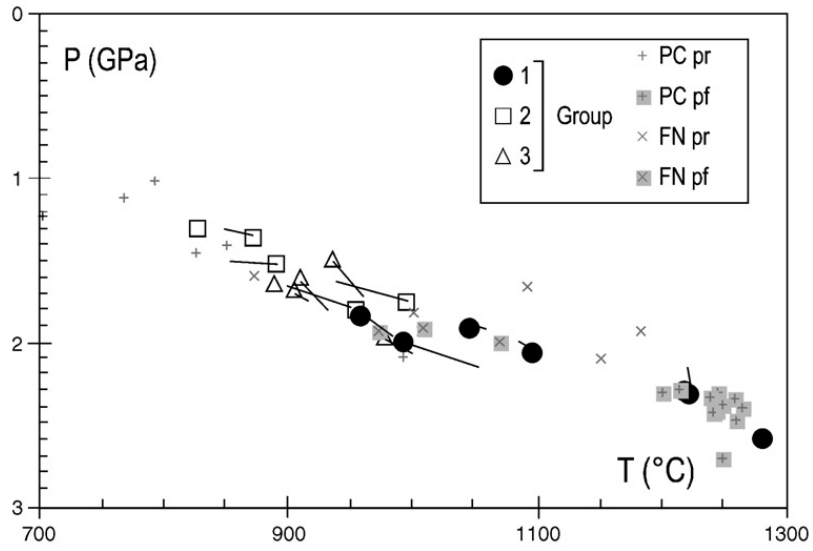

Fig. 8. Temperature–pressure variations. Geothermometer: Brey and Köhler (1990); geobarometer: Mercier et al. (1984). Tails connect the *T*, *P* values at the core crystal (symbol) and at the rim (end of the tail). Pico Cabugi (PC) and Fernando de Noronha (FN) samples (Rivalenti et al., 2000) are plotted in grey (pf=porphyroclastic; pr=protogranular).

group 3, and in the lower-*T* *group 1* samples, rim temperature is higher than that of the core (Fig. 8).

6. Discussion

The temperature–pressure variations of the three xenolith groups indicate they may represent a mantle section where the porphyroclastic *group 1* and the protogranular *group 2* were located in the hotter (possibly deeper) and colder (possibly shallower) regions, respectively, and the *group 3* xenoliths were the transition. Xenolith textures vary with all the geochemical features, such as the solid–solid element partitioning, as well as the trace element and isotope composition of the clinopyroxenes. These characteristics are similar to those found at Pico Cabugi and Fernando de Noronha by Rivalenti et al. (2000), who interpreted the xenolith suites of these localities as representing a lithospheric mantle segment which underwent deformation by asthenospheric mantle diapirs (Downes, 1990) and interaction with asthenosphere-derived alkaline melts at its base levels (corresponding to the present *group 1* xenoliths) and chromatographic enrichment only in LREE, Th and U in its shallowest levels (corresponding to the present *groups 2* and *3* xenoliths). The latter were regarded as remnants of the lithosphere predating metasomatic enrichment.

On account of the good *T*–*P* correlation illustrated in Fig. 8, this is our preferred scenario. However, we are aware that pressure estimates in spinel-facies peridotites are questionable. As an alternative end-member hypothesis, it could be envisaged that all the studied xenoliths were derived from the same lithospheric level. In this case, the *group 1* xenoliths may represent mantle regions infiltrated by high, time-integrated, melt fractions, where peridotite re-equilibrated to the melt temperature. Differently, the *groups 2* and *3* xenoliths may derive from adjacent "melt-free" regions, traversed only by small melt fractions, which preserved "fossil" lithospheric temperatures. The lack of successive thermal re-equilibration between the three groups may be a consequence of eruption just after, or during, the infiltration event. Documents of processes like the one just depicted are provided by peridotite massifs (e.g. Ronda and Lanzo, Lenoir et al., 2001; Piccardo et al., 2007-this issue), but are virtually impossible to constrain in xenoliths. In any case, the second scenario differs from the first one only in terms of depth variations and existence of a lithospheric thermal gradient, with the geochemical gradients and correlated thermal variations being similar in both cases.

We discuss in the following the records of melting-related depletions, the nature of the metasomatic enrichment process and the reasons for the different isotope characteristics between *group 1* xenoliths and the others.

6.1. Melting-related depletion

A comparison of the bulk-rock variation trends (Fig. 3) with the grid provided by Herzberg (2004), relating initial and final melting pressure and amount of basalt extraction, suggests that the present peridotites underwent ~ 10–20% melting in a pressure range of 1–2.5 GPa.

Author's personal copy

Comparison with the model trends of Niu (1997) (Fig. 3) supports up to ~ 20% melting. Nevertheless, it is also apparent in Fig. 3 that the bulk rock composition of the north-eastern Brazil ultramafics is characterised by impoverishment in SiO_2 and CaO with respect to the compositional trends induced by partial melting. These compositional features were interpreted by Niu (1997) and Asimow (1999) as the result of interaction between mantle peridotites and ascending melts.

In the *group 1* xenoliths, a melting signature is suggested by several petrochemical features, such as high bulk rock MgO content, major element variation trends in pyroxenes, higher equilibrium *T*, and low HREE content of clinopyroxenes. Constraints on the extent of melting are provided by the M-HREE concentration and fractionation of the *group 1* clinopyroxenes SV8 and BO9, which match those expected for clinopyroxene after 8 and 10% fractional melting of spinel-facies PM. If the average of LREE-depleted *group 2* composition is assumed to be the pristine peridotite affected by this process, the estimated degrees of partial melting are around 6 and 8% for SV8 and BO9, respectively. Larger degrees (12–13%) of fractional melting can be estimated on the basis of the Er–Yb concentration of clinopyroxene SV2. All the *group 1* clinopyroxenes, however, display also features inconsistent with melting processes. Besides the steadily fractionated REE pattern observed in the SV14 clinopyroxene and the convex-upward profiles of the AG7, AG8 and GR1 clinopyroxenes, which are clearly inconsistent with melting-related depletion in spinel-facies peridotites, all the others show moderate (SV8) or large enrichment of highly incompatible elements with respect to fractional melting models (Fig. 5). A process that may reconcile the evidence of fractional melting and enrichment of the highly incompatible elements, concomitant with complete re-crystallisation of the xenoliths leaving only a few deformed relics of the previous mineral assemblage, is melting triggered by the infiltration of an enriched component. In the next section it will be shown that this component is an alkali basalt. Infiltration of such a component occurred in the deeper portion of the mantle section and was favoured by shearing and deformation, as suggested by the textures of the *group 1* xenoliths. This process, previously proposed to explain the geochemical characteristics of Pico Cabugi and Fernando de Noronha porphyroclastic xenoliths (Rivalenti et al., 2000), is assumed to produce clinopyroxene compositions characterised by larger and less fractionated LREE content than that expected after near-fractional melting process only triggered by the temperature increase (e.g. Xu et al., 1998; Rivalenti et al., 2004a; Piccardo et al., 2005). These are the geochemical features observed in the trace element composition of the clinopyroxene from SV8, which, therefore, can be basically considered to reflect the geochemical consequences of the melt-assisted fractional melting process.

The development of spoon-shaped profiles in the BO9 and SV2 clinopyroxenes may be related with further percolation stages into a lithosphere sector that had already suffered melt-assisted depletion. The process details of the generation of LREE enrichments and its meaning will be discussed in the next section.

It is worth noting that significant differences also occur between the partial melting degrees estimated for *groups 2* and *3* lherzolites using alternatively bulk-rock and mineral composition. In particular, the MgO variations of bulk-rock is consistent with <1 to >15% basalt removal, whereas the overall REE fractionation of the LREE-depleted clinopyroxene is consistent with that expected after 1–2% of fractional melting of spinel-facies PM (Fig. 5). The same partial melting degrees can be argued for the rest of *groups 2* and *3* lherzolites in which the clinopyroxenes show moderate to strong enrichment in LREE because of the correspondence of the M-HREE content and fractionation. There is, therefore, a major mismatch between the depletion range indicated by bulk-rock composition and that estimated from clinopyroxene, thus suggesting that melting-related depletion is not the dominant, or the only, process recorded by the xenoliths (e.g. Rampone et al., 2004).

6.2. Metasomatic agent and process

In this section, we discuss the petrochemical evidence that:

1) variations of the clinopyroxene trace element patterns (Fig. 5) are consistent with a mantle section that underwent reactive porous flow of alkali basalts under decreasing *T*, *P* and melt/rock time-integrated ratios;
2) results of such a process vary from complete re-equilibration with the metasomatic agent in the hotter and deeper regions, to chromatographic enrichment only in the most incompatible elements (e.g. the spoon-shaped *group 3* clinopyroxenes) atop the mantle column, through transient stages close to the front of the thermo-chemical erosion, where the lithospheric peridotite is first depleted via melt-assisted partial melting and lately variably refertilised by ascending melts (Navon and Stolper, 1987; Godard et al., 1995; Zanetti et al., 1996; Vernières et al., 1997; Bedini et al.,

Author's personal copy

1997; Xu et al., 1998; Ionov et al., 2002a). The latter processes are considered to be documented by the geochemical features of the spoon-shaped *group 1* xenoliths, which are quite different in element concentrations from the *group 3* (spoon-shaped) analogues.

Discussion will be constrained by geochemical modelling.

6.2.1. Group 1

Clinopyroxene trace element patterns of the *group 1* xenoliths AG6, AG7 and GR1, recording the highest equilibrium temperatures and pressures, are typically found in peridotites that experienced interaction with infiltrating alkali silicate melts (Bodinier et al., 1988; Fabriès et al., 1989; Zanetti et al., 1996; Xu et al., 1998; Grégoire et al., 2000). The alkali basaltic nature of this component is consistently supported by the REE, Y, HFSE and Sc concentration levels and fractionation of the potential melts estimated from the clinopyroxenes AG6, AG7 and GR1, which are similar to those observed in the host alkali lavas (Fig. 9A). Complete trace element re-equilibration with the alkali basalts implies that large, time-integrated, melt volumes infiltrated the relative mantle sectors, as also supported by the low Mg# value, accompanied by high Al, Ti and Fe, of the AG6, AG7 and GR1 clinopyroxenes compared with those of the other *group 1* xenoliths (Ionov et al., 2005).

The modal and geochemical composition of wehrlite SV14 also document a mantle sector deeply affected by interaction with alkali melts. However, the clinopyroxene of wehrlite SV14 differs from those of the AG6, AG7 and GR1 for having a LREE-enriched, strongly fractionated patterns, with the highest La_n/Yb_n value, and marked negative Ti, Zr and Hf anomalies. Modal trends towards wehrlite, relative HFSE depletions and large REE fractionations are often considered as typical results of carbonatite metasomatism, which was indeed proposed by Kogarko et al. (2001) at Fernando de Noronha. Abundant literature (e.g. Bedini et al., 1997; Vannucci et al., 1998; Ionov et al., 2002a; Bodinier et al., 2004; Rivalenti et al., 2004a), however, discusses how large intra-REE and REE/HFSE fractionation can also result from alkali silicate melt metasomatism under the influence of several factors (e.g. presence of accessory mineral phases fractionating these elements, decoupling in the partition coefficients of HFSE and REE consequent to variations in the melt composition induced by the reaction) during the development of geochemical gradients connected to metasomatic process affecting lithospheric peridotites. Wehrlite is also the compositional end-member of any metasomatic process performed at lithospheric level by a *ne*-normative basalt (e.g. Zinngrebe and Foley, 1995, Peslier et al., 2002).

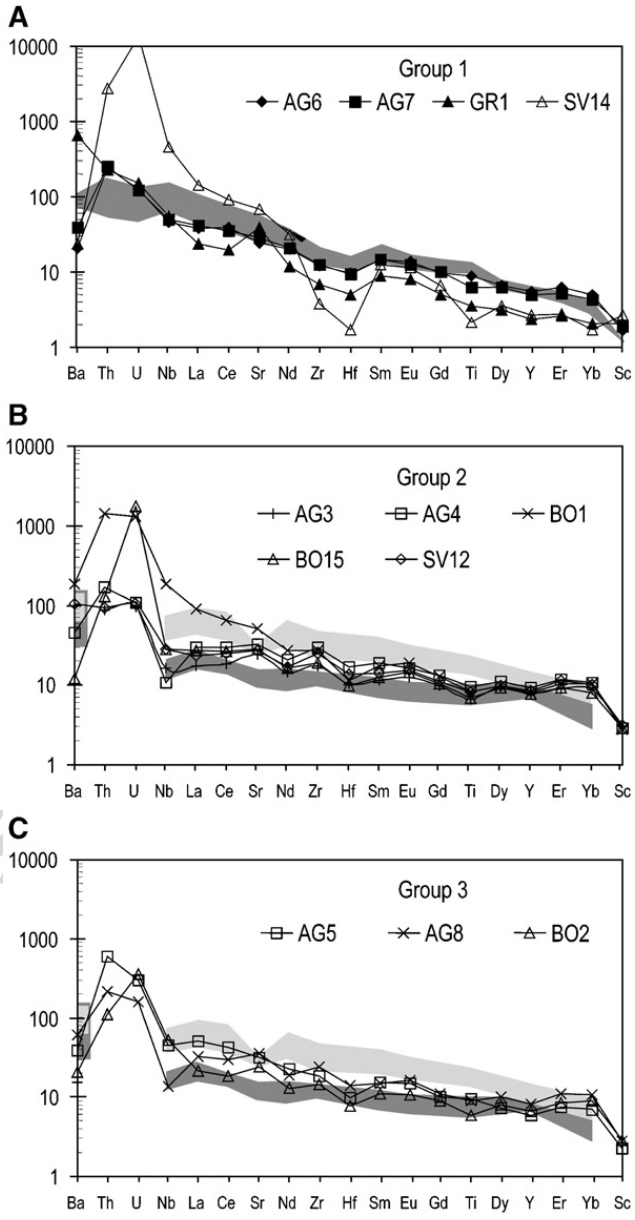

Fig. 9. A: potential melts estimated from the *group 1* convex-upward and LREE-enriched clinopyroxenes, using the partition coefficients of Hart and Dunn (1993) and those reported in Rivalenti et al. (2004b), compared with the trace element profiles of the north-eastern Brazil alkali basalts (analyses in Supplementary Table 1, see Appendix A); B and C: potential melts estimated from the *groups 2* and *3*, respectively, LREE-depleted clinopyroxene compared with the patterns of the LTi (dark-gray field) and HTi (light-gray field) Mesozoic basalts (Fodor et al., 1990). Potential melts have not been calculated from the clinopyroxenes having spoon-shaped REE patterns in *groups 1* and *3*.

Thus, we have constrained the possibility that the strong REE fractionation shown by clinopyroxene SV14 and the trend toward wehrlite can be the result of

transient geochemical gradients developed during reaction between a percolating alkali basalt and peridotite by using the Plate Model (Vernières et al., 1997). To account for the large LREE content shown by clinopyroxene SV14, it has been assumed that the infiltrating melt had the composition of the SV8 alkali basalt (Supplementary Table 1, Appendix A), which has the more LREE-rich composition so far documented in the alkaline extrusives from north-eastern Brazil. The parameters used in modelling are reported in Table 4. To match the low and fractionated M-HREE composition of clinopyroxene SV14, a strong refractory peridotite is needed (residuum after 18–20% fractional melting of DM). Such a peridotite is a clinopyroxene-poor lherzolite, and reproduction of the "wehrlitisation" process has been achieved by assuming that the melt infiltration was accompanied by assimilation of peridotite orthopyroxene and crystallisation of new olivine and clinopyroxene.

Numerical simulation successfully reproduces a mantle segment where porosity decreases upwards

Table 4
Chemical and reaction parameters used in plate model (Vernières et al., 1997) numerical modelling. Input data are reported according to Vernières et al. (1997) and Xu et al. (1998)

1. Initial peridotite (ppm)	Model 1[a]	Model 2[b]	Model 3[c]
La	6.20E− 15	5.74E− 03	7.27E− 02
Ce	2.77E− 09	1.18E− 02	2.64E− 01
Pr	9.94E− 08	3.51E− 03	4.88E− 02
Nd	1.23E− 04	3.41E− 02	3.01E− 01
Sm	1.27E− 03	2.20E− 02	1.35E− 01
Eu	1.29E− 03	8.50E− 03	5.70E− 02
Gd	7.86E− 03	3.08E− 02	1.85E− 01
Tb	2.59E− 03	6.05E− 03	3.60E− 02
Dy	2.65E− 02	4.40E− 02	2.67E− 01
Ho	7.05E− 03	1.03E− 02	6.27E− 02
Er	2.34E− 02	3.38E− 02	1.82E− 01
Tm	4.26E− 03	6.14E− 03	2.72E− 02
Yb	3.41E− 02	4.66E− 02	2.52E− 01
Lu	6.29E− 03	7.64E− 03	3.16E− 02

2. Modal parameters (weight fraction)	Ol	Opx	Cpx
Ambient peridotite Model 1	0.65	0.28	0.07
Ambient peridotite Model 2	0.74	0.22	0.03
Ambient peridotite Model 3	0.62	0.28	0.10
Crystallised minerals in Model 1	0.5		0.5
Crystallised minerals in Model 2			1
Crystallised minerals in Model 3			1
Dissolved minerals in Model 1		1	

3. Reaction parameters (weight fraction)		Model 1	Model 2	Model 3
Assimilation rate	First cell	1.00E− 03	0	0
	Last cell	1.00E− 05	0	0
Crystallisation rate	First cell	1	0.95	0.9
	Last cell	0.01	0.95	0.9
Cells number		100	20	20
Increments number		300	20	20

[a] Residual peridotite composition after 20% fractional melting of DM (Hirschmann and Stolper, 1996); melting mode at 1.5 GPa from Kinzler (1997). Mineral/liquid partition coefficients were taken by Ionov et al. (2002a).

[b] Composition and mode of spinel harzburgite GG118 (Southern Patagonian mantle), which was interpreted as the result of melt-assisted melting of lithospheric peridotites by Rivalenti et al. (2004b).

[c] Calculated from the mode of lherzolite GR3 (Ol:Opx:Cpx=0.62:0.28:0.1) by estimating olivine and orthopyroxene compositions from the partition coefficients by Ionov et al. (2002a) and the REE content of Cpx BO2.

Author's personal copy

(porosity is from 3 in the first cells down to 0.00002% at the top of the mantle column) and the initial depleted lherzolite is transformed into wehrlite.

Clinopyroxene SV14 is appreciably matched in the Pr–Lu range by the modelled clinopyroxene composition starting from the 40th cell (Fig. 10A). The relatively larger La–Ce content of clinopyroxene SV14 with respect to the model may be explained by: 1) random

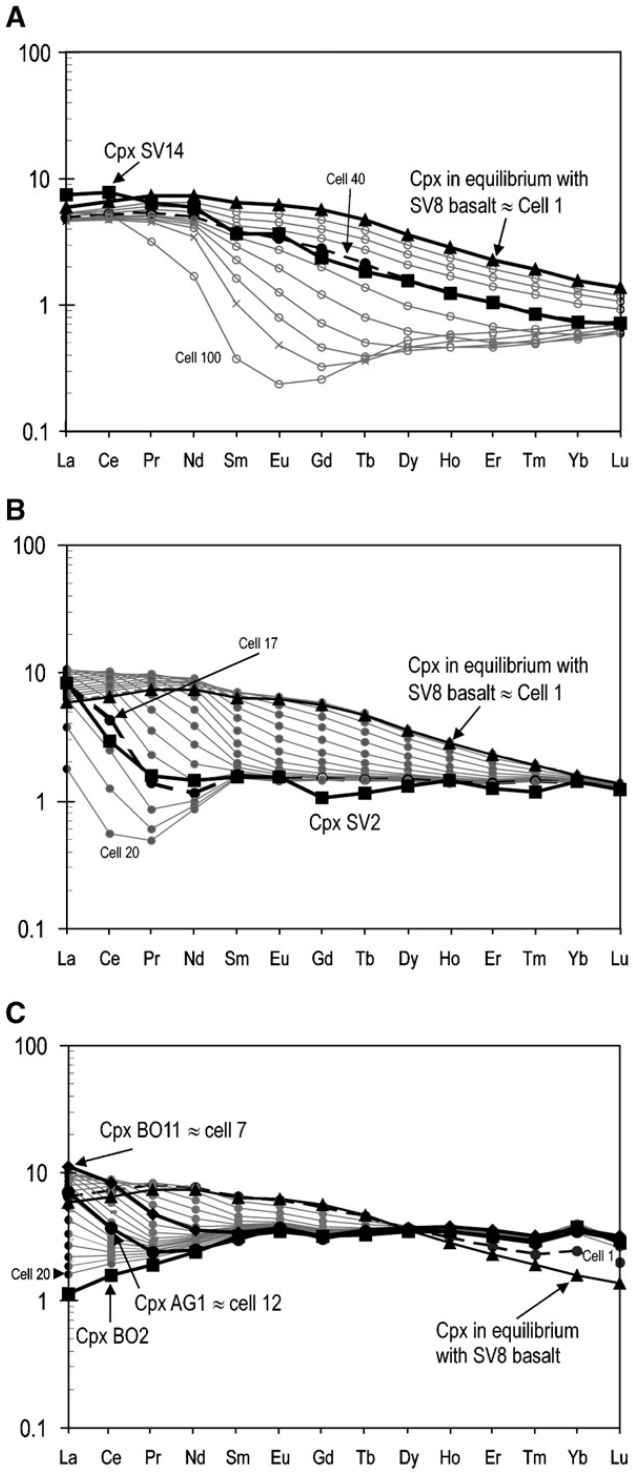

Fig. 10. Results of numerical simulation of reactive porous flow (Plate Model of Vernières et al., 1997) in comparison with REE pattern of clinopyroxenes from *groups 1* and *3* xenoliths. In the simulations, lithospheric mantle sectors of relevant compositions have been assumed to be percolated by the Cenozoic alkali basalt SV8 (Appendix A Supplementary Table 1) from the north-eastern Brazil. Initial matrix porosity was always equal to 1%. Other model parameters are reported in Table 2. Details on the scope of the different simulations and the constraints furnished by the specific results are documented below and along the text. A: this model tries to reproduce the very strong REE fractionation associated with low HREE content shown by *group 1* Cpx SV14, assuming it to reflect the development of transient geochemical composition during the melt-induced "wehrlitisation" of lithospheric peridotites. Strong MREE-HREE fractionation in SV14 clinopyroxene results from chemical re-equilibration between injected melt and ambient peridotite. The latter is believed to have had a strongly refractory character (Table 4) as a result of near-fractional melting triggered by melt injection. The PM-normalised REE patterns modelled for the clinopyroxene every 10 cells after 300 run increments are shown. Cpx from the first 10 cells have REE fractionation and absolute content very close to the chemical equilibrium with the injected melt. The REE composition of the Cpx SV14 is appreciably matched from Pr to Lu by the modelled Cpx from the 40th cell, that show a large time-integrated melt/rock ratio (≈ 0.43). The "wehrlitisation" process has been simulated by assumption that the melt infiltration was accompanied by assimilation of peridotite orthopyroxene (at decreasing rate from the base to the top of the mantle column) and crystallisation of new olivine and clinopyroxene (at increasing crystallisation rate from the base to the top of the mantle column). Final porosity varied from 3 (corresponding to the compaction limit) to 0.00002%, in the first and last cell, respectively. Mineralogical reactions varied from 1.0 $melt_1$ + 0.098 opx = 1.093 $melt_2$ + 0.003 Cpx + 0.003 Ol (at the base of the mantle column) to 1.0 $melt_1$ + 0.001 opx = 0.01 $melt_2$ + 0.4955 Cpx + 0.4955 Ol (at the top of the mantle column). B: modelling of the LREE-enriched, spoon-shaped pattern of the *group 1* clinopyroxene SV2. To match the strong LREE enrichment characterising of this sample, fractional crystallisation of the percolating melt has been assumed (according to the reaction: 1 $melt_1$ = 0.95 $melt_2$ + 0.05 Cpx) throughout the mantle column. Porosity varies from 0.4 to 0.95% at the base and at the top of the mantle column, respectively. Modelling indicates that the MREE-HREE fractionation of clinopyroxene SV2 had to be acquired before the LREE-enrichment. Possibly, it was produced during the melt-assisted partial melting suffered by *group 1* xenoliths (see text for more explanations). In the proposed solution, a refractory peridotite (Table 4) produced by such a process has been used as representative of the lithospheric composition of the specific mantle level. The model PM-normalised REE patterns for clinopyroxene are shown for 20 cells and 20 run increments. The pattern of Cpx SV2 is approached in the 17th cell (time-integrated melt/rock ratio ≈ 0.03). C: modelling of the LREE-enriched spoon-shaped *group 3* clinopyroxenes. According to petrochemical features, this kind of patterns were established on previous rather fertile lithospheric peridotites, like the *groups 2* and *3* ones with LREE-depleted clinopyroxenes. These latter were assumed to be the infiltrated peridotites (Table 4). Again, to match the LREE enrichment characterising spoon-shape distributions, it has been assumed that the melt suffered fractional crystallisation during its percolation throughout the mantle column, according to following reaction: 1 $melt_1$ = 0.90 $melt_2$ + 0.1 Cpx. Porosity varies from 0.1 to 0.9% at the first cell and at the 20th cell, respectively. The model PM-normalised REE patterns of the clinopyroxene are shown for 20 cells and 20 run increments. The spoon-shaped patterns of clinopyroxenes BO11 and AG1 correspond with the cell 7 time-integrated melt/rock ratio ≈ 0.07) and 12 (time-integrated melt/rock ratio ≈ 0.06), respectively.

variation along the column of the process parameters with respect to those used in our modelling, such as local strong decrease of the assimilation rate in the presence of a constant crystallisation rate (see the models below); 2) presence of small volumes of LREE-enriched trapped melt which, by *in situ* consumption, increases the LREE content and the LREE/HREE ratio of the minerals; 3) slightly higher LREE content of the injected melt with respect to that used in the model.

The transient nature of the LREE-enriched, spoon-shaped patterns shown by BO9 and SV2, clinopyroxenes, as well as that of clinopyroxene SV8, appears incontestable. Variable LREE enrichments associated with M-HREE-depleted clinopyroxene compositions have been documented in several world-wide mantle columns significantly modified by pervasive infiltration of alkali basalts (e.g. Grégoire et al., 2000) and were abundant among the Pico Cabugi porphyroclastic xenoliths (Rivalenti et al., 2000). As discussed in Section 6.1, the M-HREE compositions shown by SV8 and BO9 clinopyroxenes testify to the occurrence of near-fractional melting in correspondence of the thermo-chemical front of the erosion of the lithosphere.

The enrichment in LREE and other highly incompatible elements must have, instead, occurred as a relatively late event, associated with an increase of the clinopyroxene/orthopyroxene ratio (see modes in Table 1 for the samples in Fig. 5B). In particular, the REE profile of the clinopyroxene BO9 is a typical consequence of chromatographic-type impoverishment in highly incompatible elements experienced by small volumes of alkali melts percolating a refractory peridotite (e.g. Ionov et al., 2002a). However, simple chromatographic-type chemical exchange cannot account for the REE composition of clinopyroxene in SV2, because of: i) its very large La concentration, which is significantly higher than those documented in convex-upward *group 1* clinopyroxenes, considered to reflect chemical equilibrium with the ascending alkali basalts; ii) the nearly flat fractionation in the M-HREE range, which is significantly different with respect to that expected in residual clinopyroxene after partial melting.

Preliminary Plate Model numerical simulations have demonstrated that a simple chromatographic-type re-equilibration between a LREE-enriched, strongly-fractionated melt, such as that calculated in equilibrium with SV14 clinopyroxene, and refractory peridotite having strong M-HREE fractionation (like that argued by the composition of BO9 and SV8 clinopyroxenes) can reproduce the LREE enrichment and the HREE depletion documented by the SV2 clinopyroxene. Nevertheless, these calculations dramatically failed to match the flat MREE fractionation. As a whole, the large MREE content of SV2 clinopyroxene appears to be a compositional feature acquired by the peridotites before the development of the LREE enrichment, likely during melt-assisted partial melting.

To prove this hypothesis, further Plate Model simulations were performed using the composition of peridotite xenoliths from the Patagonian lithosphere considered the product of the melt-assisted partial melting (Rivalenti et al., 2004b), but showing less M-HREE fractionation with respect to SV2 and BO9 clinopyroxenes. For sake of simplicity, the SV8 alkali basalt was considered again as the infiltrating melt. The modelled gradient showing the best fit with the observed concentrations and the relevant model parameters are reported in Fig. 10B and Table 4, respectively. The modelling results suggest that, although the development of spoon-shape patterns is related to the migration of small melt volumes basically evolving through the chemical re-equilibration with the host peridotite, the LREE content of the injected melt had to be increased during the early reaction stages by its volume decrease induced by percolative fractional crystallisation. According to the observed modal variations, this process has been documented by allowing for clinopyroxene crystallisation throughout the mantle column.

6.2.2. Groups 2 and 3

Indicators of metasomatism in these peridotites are the LREE-enriched spoon-shaped clinopyroxenes of *group 3* and the slight LILE and LREE enrichment and variability shown by clinopyroxenes from other *groups 2* and *3* peridotites. The presence of melt-related heterogeneity in these peridotites has been also documented in Section 6.1 on the basis of the significant differences in terms of degrees of partial melting provided by trace element mineral chemistry and bulk rock major element composition.

The similarity of the spoon-shaped clinopyroxenes in the range Nd to Yb with the other *groups 2* and *3* clinopyroxenes suggests that metasomatism affected a lithosphere segment having dominant pre-metasomatic characteristics represented by the LREE-depleted pyroxenes of these groups. The significant increase of the LREE (but also U, Th, and sometimes Sr) concentration in the spoon-shaped clinopyroxenes can be reached by percolation of alkali basalts through the fertile lithospheric *group 2* peridotites (Model 3; parameters in Table 4 and in the Fig. 10C caption) when small melt volumes are progressively exhausted by percolative fractional crystallization. Under these conditions, the moderately incompatible trace elements

Author's personal copy

are efficiently buffered to the peridotite mineral composition, whereas highly incompatible elements can be progressively concentrated in the extremely differentiated liquids (see also Vernières et al., 1997; Xu et al., 1998).

The origin of the trace element variability in the rest of *groups 2* and *3* peridotites is more ambiguous. These characteristics may have been acquired during previous mantle processes, as suggested by the potential melts calculated on the basis of trace element composition of the *groups 2* and *3* clinopyroxenes (Fig. 9B and C), which resemble the low-Ti basalts belonging to the tholeiitic effusions that affected north-eastern Brazil during Mesozoic (Fig. 9B and C; Mizusaki et al., 2002). Further valuable evidence supporting this hypothesis is: 1) the lack of significant trace element zoning in the clinopyroxenes from these samples; 2) the lower temperature of the *group 2* clinopyroxene rims with respect to their respective cores, indicating that they did not suffer the heating event connected with the Cenozoic metasomatism; 3) the isotope array defined by the LREE-depleted clinopyroxenes (*array 2*; Fig. 7), pointing to the composition of the Mesozoic basalts.

6.3. Isotope components

The isotopic array of the *group 1* clinopyroxenes, integrated with the metasomatic model presented in the preceding section, indicates that the DM component is lithospheric (so far recorded in some protogranular peridotites), whereas the enriched EMI-like component is asthenospheric because the isotopically enriched xenoliths are the porphyroclastic GR1, SV2 and SV14 samples which experienced the highest interaction with alkali basalts. This interpretation can be extended to the host basalts, which contain a DM and an EMI component (Fodor et al., 1998), and may have acquired the DM imprint by interaction with the lithosphere during their emplacement.

The isotope-array of the LREE-depleted clinopyroxenes (*array 2*, Fig. 7) points to an enriched end-member, which is consistent with the composition of the Mesozoic tholeiitic basalts, in between EMI and EMII. The isotope composition of the alkali basalts from north-east Brazil is very close to that shown by the volcanics erupted at Fernando de Noronha. In the latter, Gerlach et al. (1987) identified, besides HIMU and DM, an EMII component and attributed it to the presence of recycled continental crust in the asthenosphere. These Authors observed in the lavas a progressive diminution of this component with time and inferred that this reservoir was progressively exhausted. In north-eastern Brazil, this high-Sr component clearly characterizes only the lithospheric xenoliths which escaped the Cenozoic metasomatic event and which isotopically trend toward the field of the Mesozoic basalts. Therefore, it is suggested that, in agreement with Gerlach et al. (1987), this component was no longer present, or was very diluted, in the asthenosphere during Cenozoic. At this time, the lithosphere recorded the EMII component as a result of ancient, probably Mesozoic, processes and its presence in the Cenozoic lavas may have been acquired by mixing of an asthenospheric (essentially EMI-like) and a lithospheric components recording a DM–EMII signature inherited from ancient events. In this scenario, *array 1* (Fig. 7) may not be a simple mixing line between a DM and an EMI component, but a mixing between the latter and a lithosphere recording variable isotopic values between DM, EMII and possibly HIMU. This may explain also the *group 1* clinopyroxenes plotting outside array 1, Pc105 and FN5.

The region labelled "*array 3*" in Fig. 7 is occupied only by spoon-shaped clinopyroxenes from north-eastern Brazil and Fernando de Noronha, which have suffered chromatographic enrichment of highly incompatible element during the Cenozoic metasomatic event (see Section 6.2.2). It is possible that small volumes of ephemeral melts, responsible for the metasomatism of these xenoliths, were enriched in Sr relative to the less incompatible Nd, thus inducing $^{87}Sr/^{86}Sr$ enrichment with respect to $^{143}Nd/^{144}Nd$, as proposed by Ionov et al. (2002b) as a result of chromatographic-type metasomatic processes.

We report in Fig. 7 the results of an assimilation–fractional crystallisation model (AFC) in the numerical version of DePaolo (1981), assuming constant isotope values in the end members ($^{143}Nd/^{144}Nd = 0.5134$ and 0.5124, $^{87}Sr/^{86}Sr = 0.7023$ and 0.7052 in the peridotite and contaminant, respectively) and $Sr/Nd = 15$ in the lithospheric peridotite. Other model parameters are reported in the Fig. 7 caption. By changing the Sr/Nd value of the contaminant from 10 to 37, the model variation curve changes from concave-upward to convex-upward, approximating the array of the *group 1* and of the spoon-shaped *group 3* clinopyroxenes, respectively. However, the Sr/Nd value assumed for the contaminant in order to obtain the convex-upward variation is very high compared with the value of the Cenozoic alkali basalts (15–18) and of OIB (17; Sun and McDonough, 1989) and is more likely explained by chromatographic processes enriching Sr with respect to Nd. This model suggests that metasomatism inducing the characteristics of the Sr-enriched group could be a final metasomatic result of the same agent that induced the *group 1* characteristics. This conclusion is also supported by the major element composition of the

Author's personal copy

group 3 clinopyroxenes and temperature, which are transitional between *groups 1* and *2*, and by the higher temperature recorded by the pyroxene rims with respect to the cores, indicating a thermal increase possibly concomitant with metasomatism.

In conclusion, the isotope variations of the present xenoliths support the hypothesis that the Cenozoic metasomatic event affected a mantle lithosphere which suffered older processes most probably related to the Mesozoic magmatism. The porphyroclastic and the protogranular Pico Cabugi and Fernando de Noronha xenoliths isotopically behave, respectively, like the *group 1* and *groups 2–3* ones of the new localities here examined, thus indicating that the previous conclusions on the differences between Fernando de Noronha and north-eastern Brazil (Rivalenti et al., 2000) were only a consequence of scarce sampling. If the isotope characteristics of the protogranular xenoliths here reported represent those of the continental lithosphere predating the Cenozoic metasomatism, then the similarity with the protogranular Fernando de Noronha xenoliths reenforces the conclusions of Gerlach et al. (1987) that the lithosphere beneath Fernando de Noronha is continental.

6.4. Plume evidence

None of the characteristics of the north-eastern Brazil xenolith suite provides unquestionable evidence of plume interference. For example, the mantle stratigraphy documented by the textural, geochemical, isotopic and thermal variations and its high geothermal gradient, often considered a typical result of plume impingement on the lithosphere (e.g. Hauri and Hart, 1994; Zangana et al., 1997; Xu et al., 1998; Mattielli et al., 1999; Sleep, 2003), are also found in other mantle sections where processes are not controlled by a plume (e.g. Vaselli et al., 1995; Witt-Eickschen and Kramm, 1997; Witt-Eickschen et al., 1998). Indeed, they may be expected any time when lithosphere records the passage of basaltic melts.

If the existence of the Fernando de Noronha plume is given as granted, the only evidence of its interaction with the north-eastern Brazil lithosphere is the similarity of isotope compositions and processes of the lithosphere of the two localities. The isotopic arrays of the porphyroclastic xenoliths (representing the mantle segment that experienced the greatest interaction with the asthenosphere-derived basalts) in both cases indicate that a lithosphere having DM and EMII characteristics was enriched by an asthenospheric basaltic melt having EMI-like characteristics. If asthenosphere melting was triggered by the addition of plume material, then the enriched component may represent a plume characteristic.

7. Conclusions

The xenoliths from the new localities of north-eastern Brazil examined in this study are samples of a mantle section ranging from a deep, high *T*, *P* region (*group 1*, porphyroclastic xenoliths) where lithosphere thermal and chemical erosion occurred, to a shallow and relatively cool region (*group 2*, protogranular xenoliths) that mainly records geochemical characteristics inherited from earlier mantle processes. The transition between the deepest and the shallower lithospheric levels is represented by a xenolith group (*3*) that shares many of the characteristics of *group 2*, but records higher temperatures in the pyroxene rims with respect to cores and is chromatographically enriched in highly incompatible elements.

The characteristics of the agent that infiltrated at the base of the lithosphere are consistent with those of an asthenospheric alkali basalt having EMI isotope characteristics. This component is specifically documented in the porphyroclastic xenoliths that experienced the largest interaction with the metasomatic agent.

The protogranular xenoliths exhibit a large range of isotope values between DM, EMI and EMII. The last component is not documented in the porphyroclastic xenoliths and thus does not appear to be asthenosphere-derived. We tentatively attribute this component to the effect of previous metasomatic episodes, possibly related to the Mesozoic magmatism.

The lithosphere stratigraphy is based on pressure estimates, which in spinel-facies peridotites may be questionable. However, even rejecting the estimated pressures, evidence remains that high temperatures are related with important geochemical and isotopic variations. Thus, all the conclusions on the metasomatic process and provenance of the isotope end-members would remain valid.

A comparison of the characteristics of north-eastern Brazil and Fernando de Noronha shows that both lithospheres record similar stratigraphy, interaction with an asthenospheric EMI component and similar heterogeneity in the cooler lithosphere section documented by the protogranular xenoliths. This similarity lends support to the relationship between the north-eastern Brazil Cenozoic magmatism and the passage of the Fernando de Noronha plume and to the notion of the presence of a detached piece of continental lithosphere beneath Fernando de Noronha.

Author's personal copy

Acknowledgements

J-.L. Bodinier and G.M. Yaxley are greatly thanked for their constructive critical review of the manuscript. J-.L. Bodinier is also thanked for having kindly provided the Plate Model software. The authors are grateful to H. Downes and H. H. G. J. Ulbrich for reviewing the manuscript and to P. Mori, M. Sugano and S. Andrade for the XRF and ICP-MS analyses on major element composition of the xenoliths and trace element concentration in the basalts. This research was financially supported by the MURST (PRIN funds) and by the Brazilian agencies FAPESP and CNPq.

Appendix A. Supplementary data

Supplementary data associated with this article can be found, in the online version, at doi:10.1016/j.lithos.2006.06.012.

References

Asimow, P.D., 1999. A model that reconciles major- and trace-element data from abyssal peridotites. Earth Planet. Sci. Lett. 169, 303–319.

Baker, M.B., Beckett, G.R., 1999. The origin of abyssal peridotites: a reinterpretation of constraints bases on primary bulk compositions. Earth Planet. Sci. Lett. 171, 49–61.

Bedini, R.M., Bodinier, J.-L., Dautria, J.M., Morten, L., 1997. Evolution of LILE-enriched small melt fractions in the lithospheric mantle: a case study from the east African Rift. Earth Planet. Sci. Lett. 153, 67–83.

Bodinier, J.-L., Dupuy, C., Dostal, J., 1988. Geochemistry and petrogenesis of eastern Pyrenean peridotites. Geochim. Cosmochim. Acta 52, 2893–2907.

Bodinier, J.-L., Menzies, M.A., Shimizu, N., Frey, A., McPherson, E., 2004. Silicate, hydrous and carbonate metasomatism at Lherz, France: contemporaneous derivatives of silicate melt–harzburgite reaction. J. Petrol. 45, 299–320.

Brey, G.P., Köhler, T., 1990. Geothermobarometry in four-phase lherzolites. II. New thermobarometers, and practical assessment of existing thermobarometers. J. Petrol. 31, 1353–1378.

DePaolo, D.J., 1981. Trace element and isotopic effects of combined wallrock assimilation and fractional crystallization. Earth Planet. Sci. Lett. 53, 189–202.

Downes, H., 1990. Shear zones in the upper mantle — relation between geochemical enrichment and deformation in mantle peridotites. Geology 18, 374–377.

Fabriès, J., Bodinier, J.-L., Dupuy, C., Lorand, J.P., Benkerrou, C., 1989. Evidence for modal metasomatism in the orogenic spinel lherzolite body from Caussou (northeastern Pyrenees, France). J. Petrol. 30, 176–199.

Faure, G., 2001. Origin of Igneous Rocks: the Isotopic Evidence. Springer-Verlag, Berlin. 496 pp.

Fodor, R.V., Sial, A.N., Mukasa, S.B., McKee, E.H., 1990. Petrology, isotope characteristics, and K–Ar ages of the Maranhão, northern Brazil, Mesozoic basalt province. Contrib. Mineral. Petrol. 104, 555–567.

Fodor, R.V., Mukasa, S.B., Sial, A.N., 1998. Isotopic and trace-element indications of lithospheric and asthenospheric components in Tertiary alkalic basalts, northeastern Brazil. Lithos 43, 197–217.

Fodor, R.V., Sial, A.N., Gandhok, G., 2002. Petrology of spinel peridotite xenoliths from northeastern Brazil: lithosphere with high geothermal gradient imparted by Fernando de Noronha plume. J. South Am. Earth Sci. 15, 199–214.

Gerlach, D.C., Stormer, J.C., Mueller, P.A., 1987. Isotopic geochemistry of Fernando de Noronha. Earth Planet. Sci. Lett. 85, 129–144.

Godard, M., Bodinier, J.-L., Vasseur, G., 1995. Effects of mineralogical reactions on trace element redistributions in mantle rocks during percolation processes: a chromatographic approach. Earth Planet. Sci. Lett. 133, 449–461.

Grégoire, M., Moine, B.N., O'Reilly, S.Y., Cottin, J.Y., Giret, A., 2000. Trace element residence and partitioning in mantle xenoliths metasomatized by highly alkaline, silicate- and carbonate-rich melts (Kerguelen Islands, Indian Ocean). J. Petrol. 41, 477–509.

Hart, S.R., Dunn, T., 1993. Experimental cpx/melt partitioning of 24 trace elements. Contrib. Mineral. Petrol. 113, 1–8.

Hauri, E.H., Hart, S.R., 1994. Constraints on melt migration from mantle plumes: a trace element study of peridotite xenoliths from Savai'i, western Samoa. J. Geophys. Res. 99, 301–324.

Hellebrand, E., Snow, J.E., Műhe, R., 2002. Mantle melting beneath Gakkel Ridge (Arctic Ocean): abyssal peridotite spinel compositions. Chem. Geol. 182, 227–235.

Herzberg, C., 2004. Geodynamic information in peridotite petrology. J. Petrol. 45, 2507–2530.

Hirschmann, M.M., Stolper, E.M., 1996. A possible role for garnet pyroxenite in the origin of the "garnet signature" in MORB. Contrib. Mineral. Petrol. 124, 185–208.

Hofmann, A.W., 1988. Chemical differentiation of the Earth: the relationship between mantle, continental crust, and oceanic crust. Earth Planet. Sci. Lett. 90, 297–314.

Ionov, D.A., Bodinier, J.L., Mukasa, S.B., Zanetti, A., 2002a. Mechanisms and sources of mantle metasomatism: major and trace element compositions of peridotite xenoliths from Spitsbergen in the context of numerical modelling. J. Petrol. 43, 1–41.

Ionov, D.A., Mukasa, S.B., Bodinier, J.-L., 2002b. Sr–Nd–Pb isotopic compositions of peridotite xenoliths from Spitsbergen: numerical modelling indicates Sr–Nd decoupling in the mantle by melt percolation metasomatism. J. Petrol. 43, 2262–2278.

Ionov, D.A., Mukasa, S.B., Bodinier, J.-L., 2005. Origin of Fe-rich lherzolites and wehrlites from Tok, SE Siberia, by reactive melt percolation in refractory mantle peridotites. Contrib. Mineral. Petrol. 150, 335–353.

Jenner, G.A., Longerich, H.P., Jackson, S.E., Fryer, B.J., 1990. ICP-MS — a powerful tool for high-precision trace-element analysis in Earth sciences: evidence from analysis of selected U.S.G.S. reference samples. Chem. Geol. 83, 133–148.

Johnson, K.T.M., Dick, H.J.B., 1992. Open system and temporal and spatial variation of peridotite and basalt of the Atlantis II Fracture Zone. J. Geophys. Res. 97, 9219–9241.

Johnson, K.T.M., Dick, H.J.B., Shimizu, N., 1990. Melting in oceanic upper mantle: an ion microprobe study of diopsides in abyssal peridotites. J. Geophys. Res. 95, 2661–2678.

Kinzler, R.J., 1997. Melting of mantle peridotite at pressure approaching the spinel to garnet transition: application to mid-ocean ridge basalt petrogenesis. J. Geophys. Res. 102, 853–874.

Kogarko, L.N., Kurat, G., Ntaflos, T., 2001. Carbonate metasomatism

Author's personal copy

of the oceanic mantle beneath Fernando de Noronha Island, Brazil. Contrib. Mineral. Petrol. 140, 577–587.

Köhler, T.P., Brey, G.P., 1990. Calcium exchange between olivine and clinopyroxene calibrated as a geothermobarometer for natural peridotites from 2 to 60 kb with applications. Geochim. Cosmochim. Acta 54, 2375–2388.

Lenoir, X., Garrido, C.J., Bodinier, J.-L., Dautria, J.-M., Gervilla, F., 2001. The recrystallization front of the Ronda Peridotite: evidence for melting and thermal erosion of subcontinental lithospheric mantle beneath the Alboran basin. J. Petrol. 42, 141–158.

LeMaitre, R.W., 1979. A new generalised petrological mixing model. Contrib. Mineral. Petrol. 71, 133–137.

Mattielli, N., Weis, D., Scoates, J.S., Shimizu, N., Mennessier, J.-P., Gégoire, M., Cottin, J.-Y., Giret, A., 1999. Evolution of heterogeneous lithospheric mantle in a plume environment beneath the Kerguelen Archipelago. J. Petrol. 40, 1721–1744.

Mercier, J.-C.C., Benoit, V., Girardeau, J., 1984. Equilibrium state of diopside-bearing harzburgites from ophiolites: geobarometric and geodynamic implications. Contrib. Mineral. Petrol. 85, 391–403.

Mercier, J.-C.C., Nicolas, A., 1975. Textures and fabrics of upper mantle peridotites as illustrated by xenoliths from basalts. J. Petrol. 16, 454–484.

Mizusaki, A.M.P., Thomaz-Filho, A., Milani, E.J., de Césero, P., 2002. Mesozoic and Cenozoic igneous activity and its tectonic control in northeastern Brazil. J. South Am. Earth Sci. 15, 183–198.

Mori, P.E., Reeves, S., Correia, C.T., Haukka, M., 1999. Development of a fused glass disc XRF facility and comparison with the pressed powder pellet technique at Instituto de Geociências, São Paulo University. Rev. Bras. Geocienc. 29, 441–446.

Navon, O., Stolper, E., 1987. Geochemical consequences of melt percolation: the upper mantle as a chromatographic column. J. Geol. 95, 285–307.

Niu, Y., 1997. Mantle melting and melt extraction processes beneath ocean ridges: evidence from abyssal peridotites. J. Petrol. 38, 1047–1074.

O'Connor, J.M., Duncan, R.A., 1990. Evolution of the Walvis Ridge-Rio Grande rise hot spot system: implications for African and South American plate motions over plumes. J. Geophys. Res. 95, 17475–17502.

Peslier, A.H., Francis, D., Ludden, J., 2002. The lithospheric mantle beneath continental margins: melting and melt-rock reaction in Canadian Cordillera xenoliths. J. Petrol. 43, 2013–2047.

Piccardo, G.B., Zanetti, A., Müntener, O., Poggi, E., Spagnolo, G., 2007. Melt/peridotite interaction in the Southern Lanzo peridotite: field, textural and geochemical evidence. Lithos 94, 181–209 (this issue).

Piccardo, G.B., Zanetti, A., Spagnolo, G., Poggi, E., 2005. Recent researches on melt-rock interaction in the Lanzo South peridotite. Ofioliti. 30, 135–160.

Rivalenti, G., Mazzucchelli, M., 2000. Interaction of mantle-derived magmas and crust in the Ivrea–Verbano zone and the Ivrea mantle peridotites. In: Ranalli, G., Ricci, C.A., Trommsdorff, V. (Eds.), Crust–Mantle Interactions. Proc. International School Earth Planet. Sci., Siena, pp. 153–198.

Rivalenti, G., Mazzucchelli, M., Girardi, V.A.V., Vannucci, R., Barbieri, M.A., Zanetti, A., Goldstein, S.L., 2000. Composition and processes of the mantle lithosphere in northeastern Brazil and Fernando de Noronha: evidence from mantle xenoliths. Contrib. Mineral. Petrol. 138, 308–325.

Rivalenti, G., Zanetti, A., Mazzucchelli, M., Vannucci, R., Cingolani, C.A., 2004a. Equivocal carbonatite markers in the mantle xenoliths of the Patagonia backarc: the Gobernador Gregores case (Santa Cruz Province, Argentina). Contrib. Mineral. Petrol. 147, 647–670.

Rivalenti, G., Mazzucchelli, M., Laurora, A., Cuffi, S.I.A., Zanetti, A., Vannucci, R., Cingolani, C.A., 2004b. The backarc mantle lithosphere in Patagonia, South America. J. South Am. Earth Sci. 17, 121–152.

Rampone, E., Romairone, A., Hofmann, A.W., 2004. Contrasting bulk and mineral chemistry in depleted mantle peridotites: evidence for reactive porous flow. Earth Planet. Sci. Lett. 218, 491–506.

Sato, K., Tassinari, C.C.G., Kawashita, K., Petronilho, L., 1995. O método geocronológico Sm–Nd no IG/USP e suas aplicações. An. Acad. Bras. Ciênc. 67, 313–336.

Sleep, N.H., 2003. Geodynamic implications of xenolith geotherms. Geochem., Geophys., Geosys. G^3 4, 1–21.

Sun, S.-s., McDonough, W.F., 1989. Chemical and isotopic systematics of oceanic basalts: implications for mantle composition and processes. In: Saunders, A.D., Norry, M.J. (Eds.), Magmatism in the Oceanic Basins. Geol. Soc. Spec. Publ., vol. 42, pp. 313–345.

Vannucci, R., Bottazzi, P., Wulff-Pedersen, E., Neumann, E.-R., 1998. Partitioning of REE, Y, Sr, Zr and Ti between clinopyroxene and silicate melts in the mantle under La Palma (Canary Islands): implications for the nature of the metasomatic agents. Earth Planet. Sci. Lett. 158, 39–51.

Vaselli, O., Downes, H., Thirlwall, M., Dobosi, G., Coradossi, N., Seghedi, I., Szakacs, A., Vannucci, R., 1995. Ultramafic xenoliths in Plio-Pleistocene Alkali basalts from the eastern Transylvanian basin: depleted mantle enriched by vein metasomatism. J. Petrol. 36, 23–53.

Vernières, J., Godard, M., Bodinier, J.L., 1997. A plate model for the simulation of trace element fractionation during partial melting and magma transport in the Earth's upper mantle. J. Geophys. Res. 102, 24771–24784.

Witt-Eickschen, G., Kaminsky, W., Kramm, U., Harte, B., 1998. The nature of young vein metasomatism in the lithosphere of west Eifel (Germany): geochemical and isotopic constraints from composite mantle xenoliths from the Meerfelder Maar. J. Petrol. 39, 155–185.

Witt-Eickschen, G., Kramm, U., 1997. Mantle upwelling and metasomatism beneath Central Europe: geochemical and isotopic constraints from mantle xenoliths from the Rhön (Germany). J. Petrol. 38, 479–493.

Xu, Y.G., Menzies, M.A., Bodinier, J.-L., Bedini, R.M., Vroon, P., Mercier, J.-C.C., 1998. Melt percolation and reaction atop a plume: evidence from the poikiloblastic peridotite xenoliths from Borée (Massif Central, France). Contrib. Mineral. Petrol. 132, 65–84.

Yang, H.-J., Sen, G., Shimizu, N., 1998. Mid-ocean ridge melting: constraints from lithospheric xenoliths at Oahu, Hawaii. J. Petrol. 39, 277–295.

Zanetti, A., Vannucci, R., Bottazzi, P., Oberti, R., Ottolini, L., 1996. Infiltration metasomatism at Lherz as monitored by systematic ion-microprobe investigations close to a hornblendite vein. Chem. Geol. 134, 113–133.

Zangana, N.A., Downes, H., Thirlwall, M.F., Hegner, E., 1997. Relationship between deformation, equilibration temperatures, REE and radiogenic isotopes in mantle xenoliths (Ray Pic, Massif Central, France): an example of plume–lithosphere interaction? Contrib. Mineral. Petrol. 127, 187–203.

Zindler, A., Hart, S., 1986. Chemical geodynamics. Annu. Rev. Earth Planet. Sci. 14, 493–571.

Zinngrebe, E., Foley, S.F., 1995. Metasomatism in mantle xenoliths from Gees, west Eifel, Germany: evidence for the genesis of calc-alkaline glasses and metasomatic Ca-enrichment. Contrib. Mineral. Petrol. 122, 79–96.

Author's personal copy